UNIVERSITÀ
DI PAVIA

FACOLTA' DI INGEGNERIA
DIPARTIMENTO DI INGEGNERIA INDUSTRIALE E DELL'INFORMAZIONE

CORSO DI LAUREA MAGISTRALE IN BIOINGEGNERIA

TESI DI LAUREA

TITOLO

Development of an Optically Compatible Micropatterned Platform for the Functional Characterization of 3D Human Cardiac Organoids

Candidata: Francesca Ceriani, MAT. 548799

Relatore: Prof. Francesco Pasqualini
Correlatore: Prof. Moises Di Sante
Dr. Alessandro Enrico

A.A. 2024/2025

Table of contents

Abstract

Cardiovascular diseases (CVDs) remain the leading cause of mortality worldwide, and their study is limited by the inability of conventional two-dimensional and animal models to meaningfully recapitulate pivotal aspects of human cardiac tissue structure and function. Human induced Pluripotent Stem Cell (hiPSC)-derived cardiac organoids (cardioids) capture key aspects of early heart morphogenesis. However, the quantification of mechanical forces generated by cardioids is limited by the lack of dedicated substrates that are both mechanically compliant (1-10 kPa) and compatible with high-resolution imaging techniques.

This thesis develops an optically compatible hydrogel platform by adapting a photopatterning gelatin methacrylate (GelMA) workflow from the Synthetic Physiology Lab (SPL) to low-molecular weight (575 Da) polyethylene glycol diacrylate (PEGDA). Compared to GelMA, PEGDA is lower cost and intrinsically non-bioadhesive, helping preserve cardioid integrity by reducing adhesion-driven disaggregation. The concentrations of PEGDA (7.5% w/w), the photoinitiator (Lithium phenyl-2,4,6-trimethylbenzoylphosphinate, LAP, 1 mg/mL), and the ultraviolet (UV) absorber tartrazine (1 mg/mL) were systematically optimized to maintain optical clarity and to define polymerization depth as a function of UV exposure dose (3-15 mJ/mm^2).

Grayscale-controlled photopolymerization produced three-dimensional cavities (~500 µm in diameter and ~300 µm depth) whose geometry and gel thickness enabled passive, reproducible positioning of single cardioids. The hydrogel thickness at the cavity bottom was designed to remain thin (<100 µm) to support high-resolution imaging and enabled the observation of cardioid-induced substrate deformations, indicating the feasibility of Traction Force Microscopy (TFM)-based mechanical readouts. The rapid, maskless workflow is compatible with standard 384-well plates, supporting scalable high-throughput screening (HTS) studies of cardiac development, disease, and therapeutic response.

Estratto

Le malattie cardiovascolari (CVDs) rappresentano la principale causa di mortalità a livello mondiale e il loro studio è limitato dall'inadeguatezza dei modelli sperimentali tradizionali. In particolare, i modelli bidimensionali e i modelli animali non sono in grado di ricapitolare in modo fedele la struttura tridimensionale e la funzionalità del tessuto cardiaco umano. In questo contesto, gli organoidi cardiaci derivati da cellule staminali pluripotenti indotte umane (hiPSC), noti come cardioidi, riproducono aspetti chiave della morfogenesi cardiaca. Tuttavia, la quantificazione delle forze meccaniche generate dai cardioidi è limitata a causa della mancanza di substrati dedicati che siano al contempo meccanicamente deformabili (1-10 kPa) e compatibili con tecniche di imaging ad alta risoluzione.

In questa tesi viene sviluppata una piattaforma di idrogel compatibile con microscopia ad alta risoluzione adattando un processo di fotopatterning basato su gelatina metacrilata (GelMA) e sviluppato presso il Synthetic Physiology Lab (SPL), al polietileneglicole diacrilato (PEGDA) a basso peso molecolare (575 Da). Rispetto al GelMA, il PEGDA presenta un costo inferiore ed è intrinsecamente non bioadesivo, in modo da preservare l'integrità strutturale dei cardioidi riducendo fenomeni di disaggregazione indotti dall'adesione al substrato. Le concentrazioni di PEGDA (7.5% w/w), del fotoiniziatore (litio fenil-2,4,6-trimetilbenzoylfosfinato, LAP, 1 mg/mL) e dell'assorbitore ultravioletto (UV) tartrazina (1 mg/mL) sono state ottimizzate in modo sistematico per garantire un'elevata trasparenza ottica e controllare la profondità di polimerizzazione in funzione della dose di esposizione (3-15 mJ/mm^2).

La fotopolimerizzazione controllata tramite modulazione in scala di grigi ha consentito la realizzazione di cavità tridimensionali (~500 μm di diametro e ~300 μm di profondità), la cui geometria e lo spessore del gel permettono il posizionamento passivo e riproducibile di singoli cardioidi. Lo spessore dell'idrogel sul fondo delle cavità è stato progettato per rimanere sottile (<100 μm), così da consentire l'imaging ad alta risoluzione e l'osservazione di deformazioni del substrato indotte dai cardioidi, suggerendo la fattibilità di readout meccanici basati su Traction Force Microscopy (TFM). L'intero processo di fabbricazione è stato realizzato su piastre a 384 pozzetti ed

è sufficientemente rapido da poter supportare screening ad alto rendimento (HTS), costituendo quindi una promettente piattaforma biomimetica per lo studio dello sviluppo cardiaco, delle patologie e della risposta terapeutica.

1 Introduction

1.1 The global burden of cardiovascular diseases (CVDs) and the necessity of human-relevant models

Cardiovascular diseases (CVDs) remain the leading cause of mortality worldwide, accounting for a substantial fraction of all deaths each year[1,2]. Beyond mortality, CVDs impose major long-term burdens on quality of life and healthcare systems[2,3]. Heart failure, in particular, is a rapidly growing public health issue, with global prevalence often estimated at roughly tens of millions of people (commonly cited at around ~64 million worldwide). Cardiomyopathies represent an important subset of myocardial disease that can contribute to heart failure and adverse outcomes, including in younger patients[2,4].

Across therapeutic areas, drug development remains inefficient: only a minority of compounds entering clinical trials ultimately reach the market, reflecting frequent late-stage failures due to insufficient efficacy and/or safety. In practice, these limitations contribute to a well-recognized predictivity gap between preclinical assays and clinical outcomes[5] (**Figure 1, A-B**).

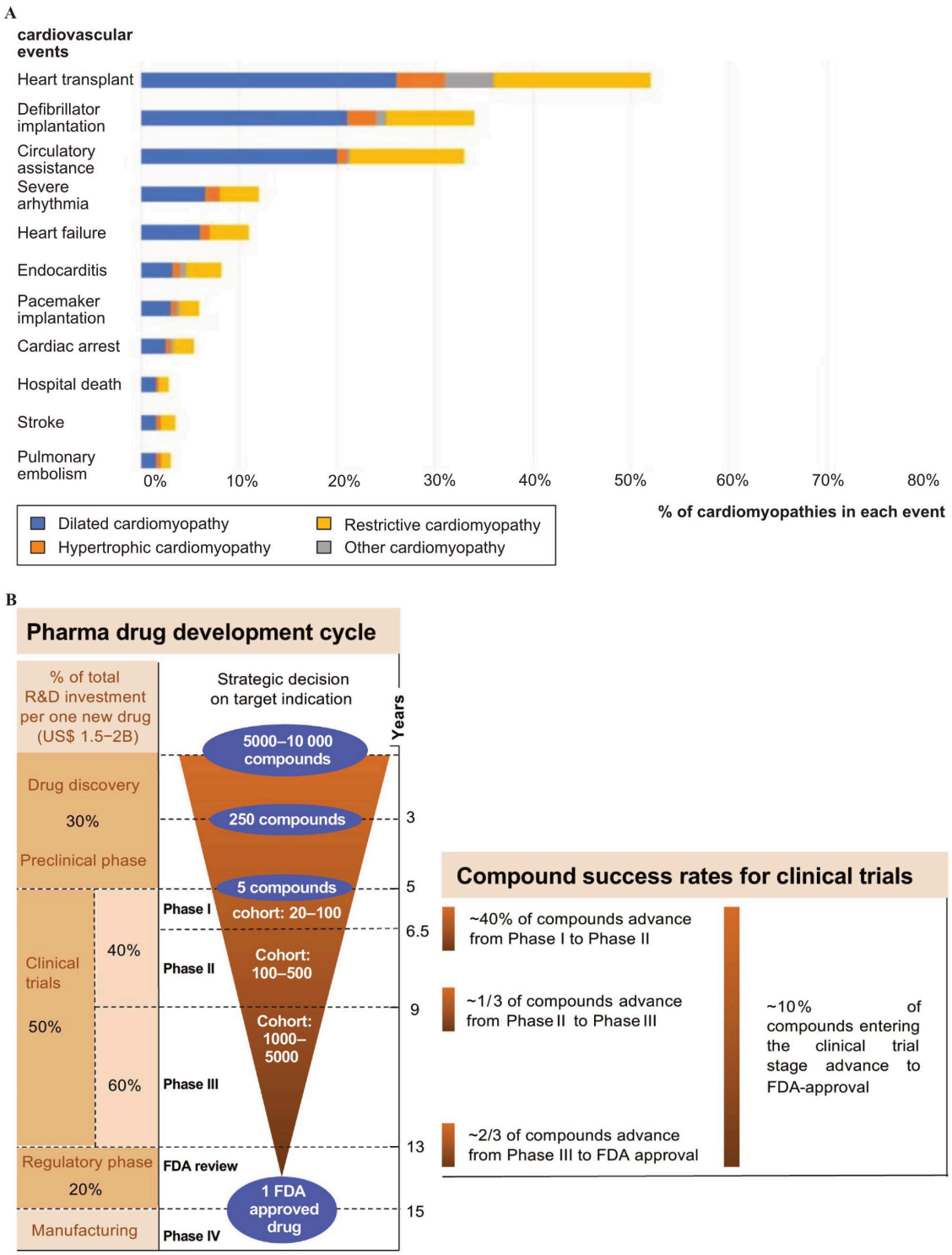

Figure 1: Clinical impact of cardiomyopathies and translational challenges in drug development

(A) Contribution of different cardiomyopathy subtypes to major cardiovascular clinical events, including heart transplantation, arrhythmias, and heart failure. Reproduced from [6]. **(B)** Schematic overview of the pharmaceutical development pipeline and compound attrition across clinical phases, highlighting the limited success rate of therapies reaching regulatory approval. Reproduced from [7].

Despite their clinical relevance, traditional preclinical models often do not fully capture key aspects of human cardiac disease progression. Animal models provide systemic physiological complexity, but species-specific differences can limit their ability to reproduce human myocardial pathophysiology and drug responses[8,9]. In parallel, conventional two-dimensional (2D) human cell cultures offer experimental accessibility but do not reproduce the three-dimensional architecture, multicellular organization, and mechanical context that shape myocardial remodelling and functional maturation[3,8,10–13]. This motivates the development of more predictive human-relevant platforms. In this context, human induced Pluripotent Stem Cell (hiPSC)-derived 3D cardiac systems, including cardiac organoids (cardioids), offer an opportunity to better capture aspects of human cardiac structure and function while remaining experimentally tractable[3,4,9–11,14–16] (**Figure 2** , **A-B**).

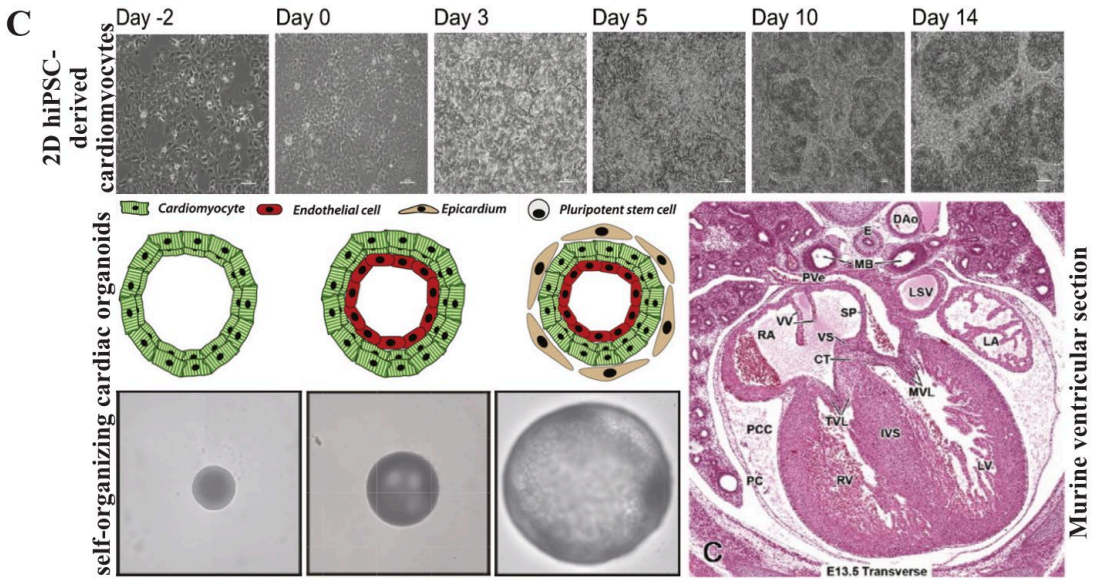

D

	2D cell culture	M. musculus	Human organoids
Ease of establishing system	✓/✗	✓	✓
Ease of maintenance	✓	✓	✓
Recapitulation of developmental biology	✗	✓	✓
Duration of experiments	✓	✓	✓
Genetic manipulation	✓	✓	✓
Genome-wide screening	✓	✗	✓
Physiological complexity	✗	✓	✓
Relative cost	✓	✓	✓
Recapitulation of human physiology	✓	✓	✓

Figure 2: Overview of cardiac model systems and their limitations

(A) Top: representative brightfield images of hiPSC-derived cardiomyocytes cultured in two-dimensional conditions across different time points. Adapted from [17]; **Bottom left:** schematic and brightfield images illustrating the generation of self-organizing cardiac organoids into three-dimensional multicellular structures. Adapted from [15]; **Bottom right:** murine cardiac tissue sections illustrating differences in structural organization and tissue-level complexity. Adapted from [8]. **(B)** conceptual comparison of physiological relevance across 2D cell cultures, animal models and human organoids. Adapted from [8].

1.2 The mechanical gap in human cardiac organoids

Although hiPSC-derived cardiac organoids (cardioids) represent a major advancement in human cardiac modelling, their functional characterization remains incomplete. Cardioids intrinsically self-organize into chamber-like, cavity-containing three-dimensional structures that recapitulate early human heart morphogenesis with significantly higher physiological relevance than conventional 2D systems[4,15]. However, while structural organization and physiological activity are routinely assessed, quantitative measurements of mechanical force generation are rarely implemented in these platforms.

Mechanical force is not merely an output of cardiac function but a central regulator of cardiac development, morphogenesis, and maturation[18,19]. Stage-specific gene regulatory networks and mechano-sensitive signaling pathways coordinate cardiac patterning and functional specification, highlighting the necessity of platforms capable of integrating morphogenetic and biomechanical readouts. In engineered cardiac tissues, biomechanical boundary conditions and substrate properties strongly influence the interpretation and quantification of contractile force measurements[20]. However, this characterization remains technically challenging, contributing to the current mechanical readout gap.

Current force-measurement strategies are largely based on bioadhesive or relatively stiff substrates that were originally optimized for 2D monolayers. These platforms often impose anchoring constraints, alter tissue morphology, or mechanically bias self-organization. Hydrogel properties can affect organoid boundary conditions and represent a critical experimental variable when designing force-measurement platforms. Studies on brain and intestinal organoids demonstrate that stiff or purely elastic matrices mechanically constrain expansion and alter lineage specification, whereas softer or stress-relaxing matrices better support physiologic development[21,22]. Similarly, bioadhesive natural matrices can introduce excessive traction constraints that perturb tissue architecture[23] (**Figure 3, A-B**).

While human cardiac organoids provide a structurally relevant model of early heart development, standardized approaches that combine mechanical permissiveness with

imaging compatibility are still emerging, and practical trade-offs remain (e.g., anchoring vs self-organization, compliance vs stability, and imaging vs long-term culture).

Collectively, these findings indicate that many existing force-sensing approaches can introduce constraints that complicate long-term culture or alter organoid shape and boundary conditions. Quantifying cardioid contractile forces commonly requires compliant, physiologically relevant substrates that reliably translate contraction into detectable deformation, while preserving mechanical stability and optical transparency.

Moreover, mechanical support should minimize bioadhesive constraints to avoid non-physiological anchoring that could influence force transmission and deformation readouts.

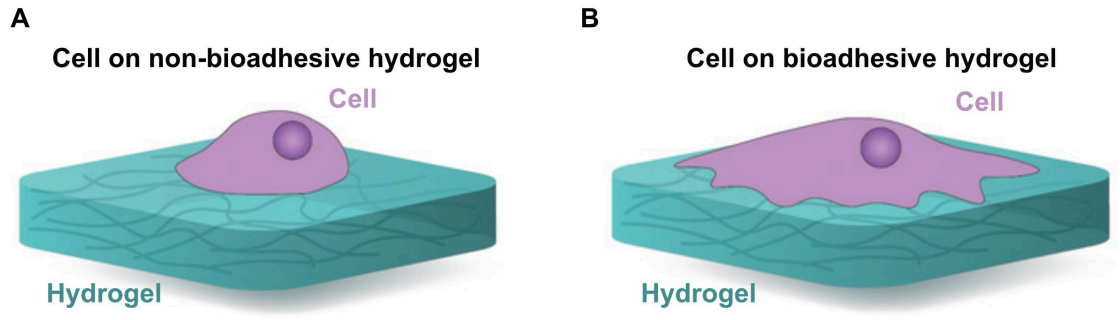

Figure 3: Conceptual representation of substrate-dependent cell spreading.

(A) Cells interacting with non-bioadhesive hydrogels exhibit limited spreading and reduced substrate contact; **(B)** cells on bioadhesive hydrogels display increased spreading. These principles are particularly relevant for organoid systems, where excessive substrate coupling may introduce mechanical constraints and disaggregation.

1.2.1 A photopatterned PEGDA platform for the functional characterization of 3D human cardiac organoids

While human cardiac organoids provide a structurally relevant model of early cardiogenesis, there is currently no standardized platform that simultaneously ensures physiological mechanical compliance, minimal bioadhesive interference, and suitable for Traction Force Microscopy (TFM). PEG-based systems represent one of the most widely used and chemically defined platforms for cell and organoid culture due to their cytocompatibility and tunable mechanical properties[24]. While unmodified PEG hydrogels are intrinsically non-bioadhesive, the addition of RGD groups can support cell adhesion (**Figure 4**, **A-B**). In this case the goal was to regulate cardioid development through matrix signaling.

A shift toward a non-bioadhesive and mechanically tunable material becomes necessary to provide a passive mechanical interface that enables stable positioning and force quantification. This thesis builds upon an existing photopatterning workflow developed in the Synthetic Physiology Lab (SPL) and adapts it to polyethylene glycol diacrylate (PEGDA, **Figure 4**, **C**). LigHTS was originally developed to enable massively parallel, biomimetic photo-functionalization of multi-well plates through digital micromirror device (DMD)-based light projection (**Figure 4 , C**), allowing spatially controlled hydrogel fabrication and patterning[9]. This approach provides maskless, programmable, and high-resolution fabrication, making it compatible with high-throughput screening. However, the original implementation used gelatin methacrylate (GelMA), a bioadhesive matrix optimized for cell adhesion, while in this work we used PEGDA for its non-cell adhesive properties.

Specifically, PEGDA hydrogels are formed through free-radical photopolymerization of acrylate end groups, leading to a covalently crosslinked network whose mechanical stiffness depends on monomer concentration, molecular weight, and crosslinking density. Under 365 nm UV illumination, the photoinitiator lithium phenyl-2,4,6-trimethylbenzoylphospinate (LAP) generates free radicals that initiate chain-growth polymerization of PEGDA acrylate groups. The addition of tartrazine as a UV photoabsorber modulated light penetration depth and enables vertical control of polymerization, allowing fine-tuning of hydrogel thickness during photopatterning. This

level of control is essential for generating thin-bottom cavities compatible with high-resolution imaging while maintaining sufficient mechanical support for organoid culture. Another key design parameter is stiffness tunability within the physiologically relevant cardiac range (approximately 1-10 kPa). This control is crucial for Traction Force Microscopy (TFM), where substrate deformability must be sufficient to transduce cellular forces into measurable bead displacements, yet stable enough to avoid excessive deformation artifacts[25]. In this work, we intentionally employ PEGDA without adhesive functionalization so that hydrogel acts as a mechanically permissive and non-instructive support. PEGDA is a chemically defined material that can improve batch-to-batch consistency compared with naturally derived matrices, although properties still depend on formulation and processing. Its inert backbone minimizes unintended cell-matrix interactions, while photopatterning compatibility allows precise spatial control of cavity geometry. Recent advances in synthetic hydrogel engineering for organoid systems further highlight the importance of matrix mechanics and architectural control in guiding morphogenesis and function[26].

Therefore, the central idea of this thesis is to adapt the LigHTS photopatterning workflow to a low-molecular weight PEGDA system combined with LAP and tartrazine. This allows us to engineer a mechanically permissive, optically compatible, and non-bioadhesive platform capable of hosting self-organizing cardiac organoids while enabling quantitative displacement-based force readouts.

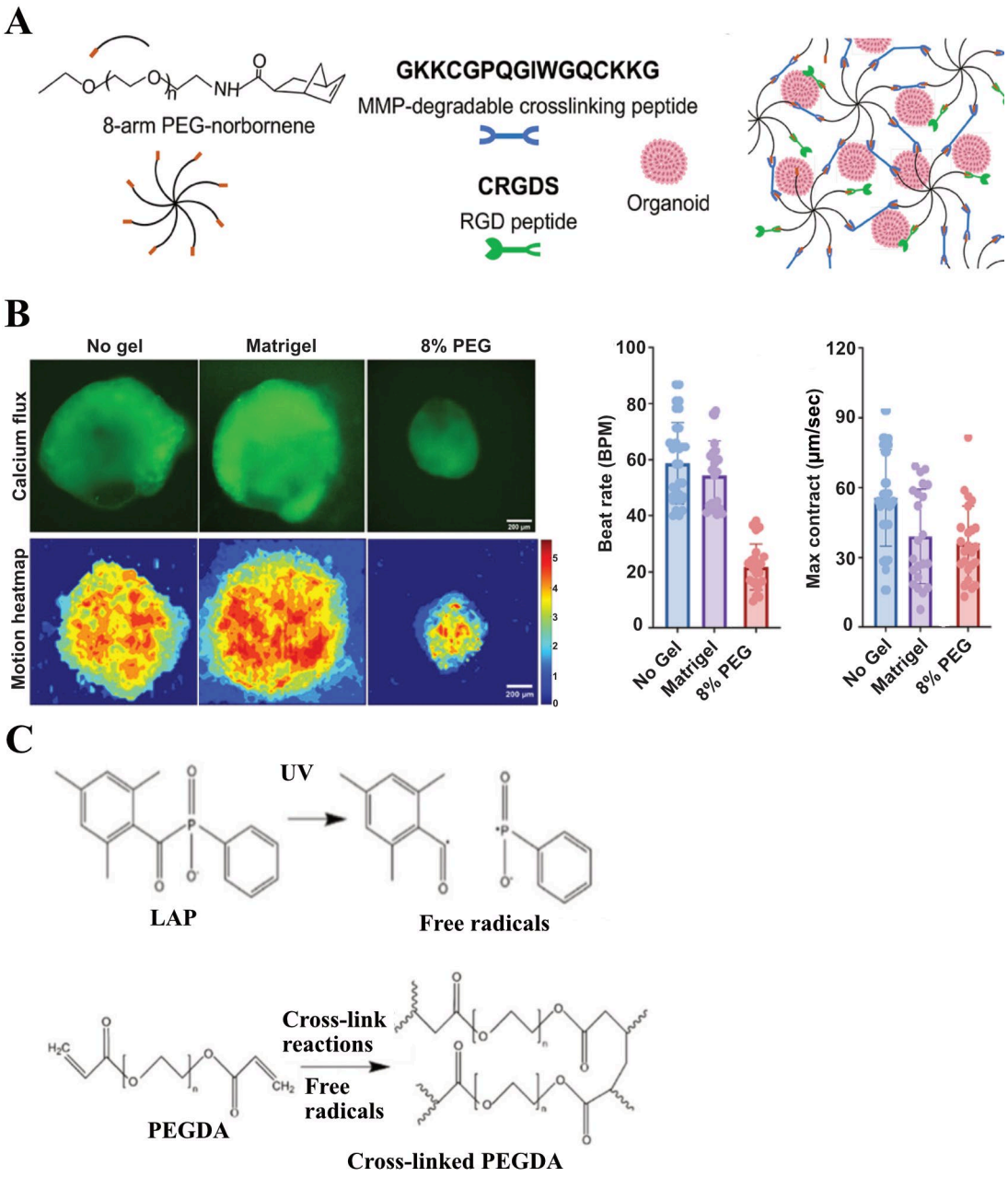

Figure 4: Synthetic photopolymerizable hydrogel platforms for organoid functional readouts.

(A) Schematic representation of modular PEG-based hydrogels incorporating bioactive ligands (RGD groups). This configuration enables precise control over cell-matrix interactions and matrix remodeling during organoid growth. Reproduced from [26]; **(B)** Representative calcium flux imaging, spatial motion heatmaps, and quantitative analysis of beat rate and maximum contraction amplitude for organoids cultures without gel, in matrigel, or in 8% PEG hydrogels illustrating differences in contraction magnitude and spatial distribution across different conditions. Adapted from [26]; **(C)** Polymerization of PEGDA where UV-activated LAP generates free radicals that drive acrylate crosslinking and network formation. Adapted from [24].

1.2.2 Traction Force Microscopy principles and adaptation to 3D cardiac organoids

Traction Force Microscopy (TFM) is a quantitative methodology for estimating the forces exerted by adherent cells on a deformable substrate. In its classical 2D configuration, fluorescent beads are embedded near the gel surface and act as fiduciary markers. Comparing bead positions between a reference state and a deformed state yields a displacement field. Traction stresses are then estimated by solving an inverse elasticity problem that links displacements to surface tractions[27,28].

The interpretation of TFM relies on modelling assumptions. The substrate is typically treated as linear elastic and isotropic. It is defined by a Young's modulus (E) and a Poisson's ratio (ν). The reconstruction often assumes a thick elastic half-space or applies corrections if the gel thickness is comparable to the deformation length scale. In standard 2D TFM workflows, only in-plane bead motion is measured. As a result, the output primarily reflects the in-plane traction components. Out-of-plane deformation and traction cannot be directly reconstructed without 3D imaging[29,30].

Recent methodological reviews provide updated guidance on experimental design, noise filtering, and reconstruction accuracy in TFM workflows[29,31] (**Figure 5 , A**). TFM has been progressively extended to multicellular and collective systems. This enables quantification of tissue-level traction stresses during coordinated migration and mechanical coupling[32,33]. Three-dimensional aggregates can induce measurable matrix deformations even in the absence of a macroscopically visible contraction. The net actomyosin-driven contractility of aggregates generates displacement fields in the surrounding matrix. The displacement field illustrated in **Figure 5-B**[34] exemplifies how multicellular tumor spheroids can remodel the substrate during their aggregation.

Nevertheless, applying TFM to beating cardiac systems introduces additional challenges. Contractile cardiomyocytes and engineered cardiac constructs generate cyclic forces, complicating the identification of a true stress-free reference configuration. Time-resolved acquisition is essential to capturing contraction-relaxation dynamics, but it increases sensitivity to stage drift and imaging noise. Furthermore, small displacement amplitudes relative to background fluctuations and the potential viscoelastic behavior of soft substrates can influence the accuracy of stress

reconstruction. Recent work addressing dynamic traction measurements in cardiac tissues highlights the need for phase-resolved acquisition strategies and careful regularization under cyclic loading conditions[34] (**Figure 5**).

Within this framework, this work employs TFM as a Proof-of-Concept (PoC) mechanical readout integrated into a photopatterned PEGDA platform engineered for self-organizing cardiac organoids. We fabricated a thin, compliant hydrogel layer with a cavity geometry to accommodate a three-dimensional beating cardioid. This configuration bridges classical planar TFM and the organoid-compatible platform. It preserves optical accessibility and minimizes adhesive constraints.

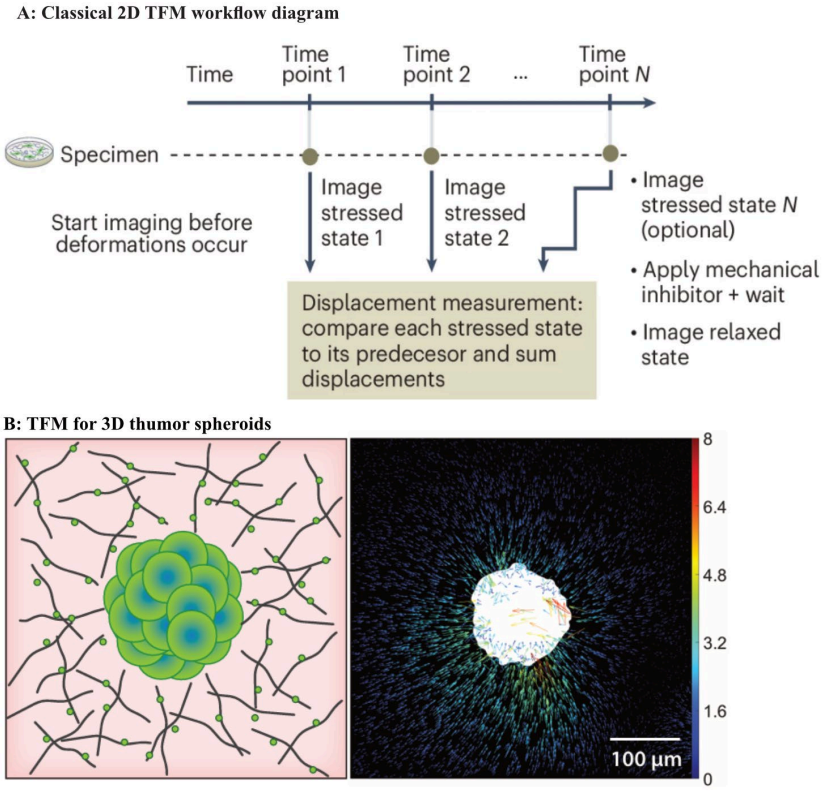

Figure 5: Traction Force Microscopy principles and adaptation to multicellular 3D models.

(A) Classical two-dimensional Traction Force Microscopy (2D TFM) workflow. Reproduced from [31]; **(B)** extension of TFM to three-dimensional multicellular systems such as tumor spheroids. Left: schematic representation of a spheroid embedded in a deformable matrix containing fluorescent beads. Right: representative displacement vector field surrounding a contracting spheroid, with color-coded magnitude scale (Pa-kPa range) and radial deformation patterns. Reproduced from [34].

1.3 Aim of the work

The goal of this thesis is to develop a photopatterned PEGDA hydrogel platform for 3D cardiac organoids (cardioids). The platform is designed to confine cardioids in defined microcavities while remaining compatible with optical imaging and deformation-based mechanical readouts.

To reach this goal, the work is organized into four objectives. First, a reproducible protocol is established to generate and characterize hiPSC-derived cardiac organoids. This provides a consistent biological model to assess compatibility with the engineered substrates. Second, the LigHTS photopatterning workflow[9] is adapted to a low-molecular weight PEGDA formulation. Polymer content, photoinitiator concentration, UV dose, and light penetration control are tuned to balance thickness control with optical transparency. Formulation and exposure settings are selected to target a compliant gel suitable for mechanical testing. Third, grayscale DMD-based photopatterning is used to fabricate 3D cavity geometries that can passively accommodate cardioids. This step focuses on achieving reliable cavity fidelity and confinement without active mechanical positioning. Finally, traction force measurements are performed as a Proof of Concept (PoC). Displacement fields reconstructed from bead motion are processed using established inversion algorithms derived from classical TFM theory [30].

Overall, this work seeks to bridge advanced human cardiac organoid models with quantitative biomechanical analysis. It provides a practical foundation for future mechanobiology studies and more predictive in vitro cardiac platforms.

2 Materials and methods

2.1 hiPSCs maintenance

Human Induced Pluripotent Stem Cells (hiPSC) were maintained in complete Essential 8 Flex Medium (A2858501, ThermoFisher Scientific) supplemented with Penicillin/Streptomycin (P/S) (A001, HiMedia) on 1:100 Growth Factor Reduced (GFR) Matrigel (7-10 mg/mL, depending on the lot), phenol red-free (356231, Corning). When reached 70% confluency (usually in 3-4 days) cells were detached using 0.5 mM Ethylenediaminetetraacetic acid (EDTA, Life Technologies) in Dulbecco's PBS (DPBS) without Ca^{2+} or Mg^{2+} (C-40232, PromoCell) for 5 min at 37°C and 5% CO_2 environment. Subsequently, cells were expanded in 6-well plates by passaging 1:10 in the presence of RevitaCell (100x, A26445-01, Life Technologies). After 24 h, the medium was replaced with complete Essential 8 Flex Medium, without RevitaCell, and changed every other day. [16]

2.2 Generation of 3D self-assembling human heart organoids

To generate cardiac organoids (cardioids) from hiPSC cells, we used the protocol described in Schmidt et al[4] and Balmas et al[35] with minor changes. Briefly, for the Anterior Primitive Streak (APS) induction (day -1), hiPSC cells were seeded at 50.000 cells per well (Matrigel-coated 24-well plate) in the presence of Essential 8 Flex + Y-27632 dihydrochloride, 5 µM (004CA16644, Cayman Chemicals).

After 24 h, the supernatant was removed and replaced with 1 mL APS-induction medium per well (Table 2), and cells were incubated at 37°C and 5% CO_2 for 36-40 h. On day 1.5, cells were detached, counted, and resuspended in CardMeso-ROCKi (Table 2) to a final concentration of 15.000 cells per well (Nunclon sphera 96-Well, U-Shaped-Bottom Microplate, 174929, Thermo Scientific). Cells were centrifuged at 200 xg for 4 min and incubated at 37°C and 5% CO2 for 24 h. From day 2.5 to 4.5, the medium was changed every day, and wells were filled with CardMeso-induction medium without ROCKi. From day 5.5 to 6.5, the medium was exchanged for CardMyo-induction

medium (Table 2). Organoids started beating at this stage. From day 7.5, the supernatant was exchanged for CardMaint medium (Table 2) and replaced every 48 h.[16]

Table 1: list of key growth factors, small molecules, and media supplements employed during hiPSC maintenance and cardiac differentiation.

Reagent name	**Supplier and # catalog number**
Bovine serum albumin (BSA)	Stem Cell Technologies, #100-0177
Optiferrin	Invitria, #777TRF029
Human FGF2-G3	Qkine, #Qk053
Activin A1	Qkine, #Qk001
BMP4	Qkine, #Qk038
Insulin	Thermo Scientific, #A11382II
Y-27632 dihydrochloride (ROCK inhibitor, ROCKi)	Cayman Chemicals, #004CA16644
LY 294002 hydrochloride	Selleckchem, #1105
CHIR99021	Cayman Chemicals, #004CA13122
C59	Cayman Chemicals, #16644
Retinoic acid	Sigma Aldrich, #R2625
F-12	Thermo Scientific, #31765068
IMDM	Thermo Scientific, #21980032
Chemically defined lipid concentrate	Thermo Scientific, #11905031
Mono-Thio-Glycerol (MTG)	Sigma-Aldrich, #M6145

Table 2: Formulation of stage-specific media used throughout the differentiation protocol, reporting components and final concentrations.

Medium	Reagent	Final Concentration
CDM	BSA	0.3%
	IMDM	~ 50%
	F-12	~ 50%
	Conc. Lipids	1%
	MTG	0.004%
	Optiferrin	15 µg/mL
APS – Induction (CDM-FLyABCh) 200 µL/96w, 20 mL/plate	**CDM**	
	FGF2-G3	6 ng/mL
	LY294002	5 µM
	Activin A1	5 ng/mL
	BMP4	8 ng/mL
	CHIR99021	5 µM
CardMeso – Induction (CDM-BFIC59Ra) 200 µL/96w, 80 mL/96wp	**CDM**	
	BMP4	8 ng/mL
	FGF2-G3	1.6 ng/mL
	Insulin	10 µg/mL
	C59	2 µM
	RA	50 nM
	Y-27632 **Day 1.5 only**	5 µM
CardMyo – Induction (CDM-BFI) 200 µL/96w, 40 mL/96wp	**CDM**	
	BMP4	8 ng/mL
	FGF2-G3	1.6 ng/mL
	Insulin	10 µg/mL
CardMaintenance (CDM-I) 200 µL/96w, 20 mL/96wp	**CDM**	
	Insulin	10 µg/mL

2.3 Substrate preparation for hydrogel anchoring

To increase PEGDA hydrogel adhesion on glass-bottom 384-well plates (P384-1.5H-N, Cellvis), the glass substrates were cleaned and silanized before casting.

Specifically, wells were incubated at room temperature for 1 h with 2% v/v Hellmanex^{TM} III (Z805939, Sigma-Aldrich) in sterile-filtered DI water, rinsed 3x with 37°C DI water, and dried.

The glass bottom of the wells was then silanized using 3-(trimethoxysilyl)propyl methacrylate (TMSPM, 440159, Sigma-Aldrich): 0.4% v/v TMSPM in aqueous solution at pH 3.5 (glacial acetic acid, 33209-M, Sigma-Aldrich). Wells were incubated with the TMSPM solution 1 h at room temperature, rinsed 3x with 37°C DI water and dried [9].

To allow the identification of the gel-glass interface by confocal fluorescence microscopy, the silanized substrates were coated with fluorescent beads. FluoSpheres^{TM} (carboxylated-modified, 0.2 µm, dark red, F8807, Invitrogen) were sonicated (minimum 30 min) and added 1:10.000 in ethanol and dispensed into the wells (50 µL per well). Then plates were centrifuged for 5 min at 1500 g to promote beads deposition. Wells were dried, and plates were used immediately or sealed (Parafilm, 11772644, Fisher Scientific) and stored at RT ≤ 1 week.

2.4 Preparation of PEGDA hydrogel precursor solution

To produce PEGDA hydrogels for UV photopolymerization, we prepared aqueous solutions of Poly(ethylene glycol) diacrylate (PEGDA, average M_n 575, 437441, Sigma-Aldrich) with photoinitiator (lithium phenyl-2,4,6-trimethylbenzoylphosphinate, LAP, 900889, Sigma-Aldrich) and UV absorber (tartrazine, T0388, Sigma-Aldrich).

To evaluate the impact of tartrazine concentration on the polymerized gel thickness, we varied the concentration of tartrazine in the PEGDA solutions, fixing the LAP concentration to 1 mg/mL. Specifically, LAP was mixed in sterile-filtered DI water. Then, the required amount of tartrazine (from 1 mg/mL to 15 mg/mL) was added to the LAP solution and vortexed until fully dissolved. The required amount of PEGDA (7.5%

w/w, 15% w/w, 30% w/w, 60% w/w, 90% w/w) was weighed and added to the solution, followed by magnetic stirring for 20 min, protected from light.

2.5 Hydrogel photopatterning

Gel patterning was performed using a PRIMO maskless digital micromirror device (DMD) system (Alvéole) mounted on a Nikon ECLIPSE Ti2 inverted microscope and controlled via Leonardo software (v2.4, Alvéole). UV illumination patterns were projected through a 4x air objective (CFI Plan Fluor 4x, N.A. 0.13, MRH00045), enabling spatially resolved photopolymerization of photosensitive hydrogel precursors.[9] Three-dimensional topographical features were generated by grayscale-controlled UV exposure, whereby local polymerization depth was modulated by varying the delivered UV dose across the projected pattern. Each pattern incorporated a 9-level grayscale modulation, corresponding to 10%-90% of the nominal UV dose in 10% increments. This approach allowed continuous control over gel thickness and cavity depth without altering the chemical composition of the hydrogel.

For each experimental condition, N = 3-4 hydrogels were fabricated. Nominal UV exposure doses ranged from 5 to 50 mJ/mm^2, depending on the design iteration, with grayscale modulation applied identically across doses. The first patterning design consisted of PEGDA "housing" cavities intended to passively capture and position cardioids. Patterns were fabricated using nominal UV doses of 5, 10, 25, and 50 mJ/mm^2, each combined with the 9-level grayscale modulation described above.

To improve positioning efficiency while avoiding high UV doses, a second design iteration focused on geometrical optimization rather than increased exposure. Based on prior results, nominal UV doses of 8 mJ/mm^2 and 15 mJ/mm^2 were selected, as these conditions yielded better cavity depth at low grayscale levels (10% illumination).

Three design variants were generated, featuring nominal truncated cone base diameters of 450 µm, 500 µm, and 550 µm. In contrast to the sharp step-like transitions used previously, these designs incorporated continuous vertical gradients between the gel surface and cavity. For each design variant, N = 4 hydrogels were fabricated at both exposure doses.

2.6 Hydrogel development, UV flooding, PLL functionalization, and preparation for cardioids

After exposure, the development was performed by incubating the gels for 30 min in warm (37°C) MES buffer (25 mM, pH 6.0 ± 0.1, 76039, Sigma-Aldrich), prepared from 0.5 M stock in DI water with NaOH (S2770) pH correction to remove uncured PEGDA and tartrazine. After the third rinse, gels were left overnight at 37°C.

Then, we added a 1 mg/mL LAP solution in MES, and the plates were flood exposed using a commercial UV LED nail lamp (365 nm, > 10 mW/cm^2) for 15 min. Then, gels were rinsed 3x with 37°C MES buffer [9]. To enable stable deposition of beads for imaging-based readouts, we coated the gel surface with poly-L-lysine (PLL, P4707, Sigma-Aldrich; 0.0025% w/v in MES) for 30 min at RT. Carboxylated polystyrene beads were diluted 1:1.000 in MES, dispensed 50 µL per well, and the plates were centrifuged 5 min at 500 x g to accelerate sedimentation. After gentle aspiration of non-adsorbed beads, a 1:1 MES in PBS -/- (Dulbecco's phosphate buffered saline, C-40232, PromoCell) solution rinse was performed. For final equilibration, 50 µL of PBS was added to each well, and plates were incubated for minimum 1 h at 37°C.

2.7 Cardioids seeding

The gels were sterilized by overnight incubation at 37°C in RPMI-1640 (1X) medium without L-Glutamine and without Phenol Red (32404-014, Sigma-Aldrich) supplemented with B-27 Minus Insulin (50X, A18956-01, Sigma-Aldrich) with 1:500 Primocin, to prepare hydrogels for cardioid seeding.

Prior to cardioid seeding, hydrogels were washed twice with PBS to remove residual medium. Individual cardioids were then gently aspirated using a P1000 pipette. A total volume of 80 µL containing a single cardioid was collected and then transferred into the well of a 384-well plate containing the hydrogel. Following dispensing, the presence of the cardioid and its correct position were verified using an Echo Revolve imaging system.

2.8 Image acquisition

2.8.1 Microscopy platforms and general configuration

Brightfield and fluorescence image acquisitions were performed on a widefield Nikon Ti2 inverted microscope with a CrestOptics X-Light V3 spinning disk confocal unit and an environmental chamber (Okolab Bold Line; 37°C, 5% CO2, humidity). The microscope is equipped with a Nikon linear-encoder motorized stage with a 200 µm range Z-piezo insert (Mad City Labs, catalog# NI-2-C312). Illumination was provided by the Lumencor Celesta light engine (405, 446, 477, 520, 546, 638, 740 nm; up to 800 mW), routed through multiband dichroics and appropriate emission filters.

The dichroic mirror wheel was selectively positioned with either a hard-coated Full Multi Band Penta CELESTA -DA/FI/TR/Cy5/Cy7-A (Nikon, catalog# MXR00543) or a Full Multiband dual CELESTA -CFP/YFP-A (Nikon, catalog# MXR00544). Depending on the excitation line, the beam was subsequently filtered through either a Multiband Full Penta FF01-391/477/549/639/741 (Semrock, catalog# FL-416877) or a Full Multiband Dual FF01-449/520 (Semrock, catalog# FL-411981).

Emission was collected using single-band filters mounted in the wheel: FF01-484/561 (Semrock, catalog# FL-412124) for CFP, FF01-685/40-25 nm (Semrock. Catalog# FL-011482) for the iRFP signal, FF01-595/31 (Semrock, catalog# FL-004391) for RFP, or FF01-511/20-25 (Semrock, catalog# FL-004306) for EGFP.

Fluorescence was captured with the same Teledyne Photometrics Kinetix CMOS camera (6.5 µm pixels; 16-bit; native resolution 3200 x 3200 pixels, cropped to 2700 x 2700 pixels). Acquisition and hardware synchronization were controlled through NIS-Elements AR (v.5.42.03). Data were stored as .nd2 files.[10]

2.8.2 Gel thickness and profile characterization by confocal microscopy

Gel thickness and bead-layer profiles were characterized using spinning-disk confocal fluorescence microscopy (Crest V3 X-Light on Nikon Ti2) coupled to a CELESTA Light Engine and a Kinetix sCMOS camera. Confocal Z-stacks to reconstructed the 3D

hydrogel structure were acquired with a 4 x 4 binning. Objective magnification and axial sampling were selected based on expected gel thickness: 4x air (Δz = 30 μm), 10x air (Δz = 5.6 μm, 3 x 3 tiled acquisitions), and 20x air (Δz = 0.9 μm, 6 x 6 tiled acquisitions).

2.8.3 Widefield fluorescence imaging

Static widefield acquisitions were performed using a CFI Plan Fluor DIC 25x (air objective, NA 1.05, catalog# MRH00105). FITC-channel time-lapse imaging was acquired using 477 nm excitation at 2% laser power, 2 x 2 binning, and 10 ms exposure time. Time-lapse sequences consisted of up to 998 frames acquired at 10 s intervals, with a resulting spatial calibration of 0.54 μm/pixel.

2.8.4 Calcium imaging

Intracellular calcium dynamics were analyzed by collecting the signal from the genetically encoded calcium reporter (GCaMP) using a CFI Plan Fluor DIC 10x air objective (N.A. 0.3, WD 16 mm, catalog# MRH00105) in widefield mode, corresponding to a pixel size of 2.69 μm/pixel in x and y. Fluorescence was recorded under 477 nm excitation with 4 x 4 binning and 10 ms exposure time. Acquisition was performed with no inter-frame delay, resulting in an effective sampling frequency of ~100 Hz.

2.8.5 Brightfield imaging

To qualitatively visualize cardioids contraction, brightfield images were acquired in widefield mode using 10x objective. Images were acquired with 10 ms exposure time, typically with 4 x 4 or 1 x 1 binning. For multipoint acquisitions, two Z-positions (“top” and “bottom”) were recorded per field of view.

2.8.6 Spinning-disk confocal Z-stack imaging

Three-dimensional confocal imaging was performed using spinning-disk confocal microscopy with 10x air objective or 25x silicone oil objective. Z-stacks were acquired using a Z-step size ranging from 4 µm to 6 µm. Single- and dual-channel acquisitions were performed in SD 520 nm and SD 638 nm channels using sequential excitation.

2.8.7 Time-lapse spinning disk confocal imaging

Time-lapse confocal imaging was performed primarily in the SD 638 nm channel using the 25x silicone oil objective. Acquisitions were conducted at 5-10 s intervals, with exposure times between 30 and 100 ms and 1 x 1 binning. Focus stability was maintained using Nikon Perfect Focus (PFS) throughout all acquisitions.

2.9 Image processing and Analysis

Raw acquisitions were denoised using NIS AI denoise tool and deconvolved using the Richardson-Lucy Algorithm (10 iterations).

All image processing and analysis were performed using Fiji (ImageJ). Raw microscopy files were imported using the *Bio-Formats Importer*. For time-lapse acquisitions, the Open all series option was enabled to ensure complete loading of multi-series datasets.

Image LookUp Tables (LUTs) were linearly adjusted to the full dynamic range of the signal without altering raw pixel values. Images were then spatially cropped to the region of interest (ROI). For dynamic image sequences, impulsive noise was reduced using the built-in *Despeckle* filter, and individual series were concatenated into a single time sequence.

For three-dimensional datasets, z-stacks were processed using *Z project* with *Average Intensity projection*. Additionally, *3D Project (Brightest Point)* was applied to generate projections along the three acquisition axes (XY, XZ, YZ), corresponding to the three recorded videos. The z-step size during acquisition was 6 µm, and this value was retained for all downstream analysis.

Temporal information was overlaid using a laboratory-developed macro that adds a time stamp based on the acquisition frame rate. The frame rate (frames per second, fps) was verified using the *ImageJ Properties* function (Ctrl+P) and converted to milliseconds to ensure that the final rendered videos had a minimum duration of 10 seconds.

For visualization and analysis of structural features, optimal focal planes were identified using *Orthogonal Views* on the *XZ and YZ planes*, where the well structure was most clearly resolved. All processing steps were applied uniformly across samples to ensure comparability and reproducibility.

2.9.1 Calcium signal image processing and quantitative analysis

Calcium imaging data were analyzed using Fiji (ImageJ). Time-dependent signal decay was first corrected using the *Bleach Correction* algorithm (*Exponential Fit*), due to fluorescence quenching of the calcium indicator upon excitation at 477 nm.

Subsequently, a Region of Interest (ROI) was manually selected on the corrected image and mean fluorescence intensity values over time were extracted using the *Time Series Analyzer* plugin (*Get Average*). The resulting fluorescence traces were exported and processed in Microsoft Excel. For each acquisition, three columns were generated: exposure time expressed in ms, raw fluorescence intensity values obtained from ImageJ, and normalized fluorescence values to enable comparison across independent recordings. Normalization was performed according to the equation:

$$(F_i - F_0) / (F_{max} - F_0)$$

where F_i is the fluorescence intensity at each time point, F_0 is the minimum value of fluorescence, and F_{max} is the maximum fluorescence value. Normalized traces were plotted as a function of time (seconds) to generate calcium transient profiles.

For quantitative characterization of calcium dynamics, normalized signals were further analyzed in ImageJ using the *Spiky* plugin for peak detection and *Peak Analysis*.

All analysis steps were applied consistently across samples to ensure reproducibility and comparability.

2.9.2 Quantification of hydrogel height by confocal image processing

Hydrogel thickness was quantified from confocal z-stack images using a custom, laboratory-developed Fiji (ImageJ) macro based on Bio-Formats. Briefly, nd2 image stacks were batch imported and pre-processed to remove initial slices when required, then resliced along the orthogonal axis using voxel dimensions extracted from image metadata. For each resliced stack, a median Z-projection was generated to obtain a single TIFF image representing the full gel cross-section.

Hydrogel height was measured manually, defining a Region Of Interest (ROI) including the gel profile and converting pixel distances into physical units based on the voxel depth calibration. To validate the accuracy of this approach, height measurements obtained from the processed projections were cross-checked against direct inspection of the original nd2 z-stacks by identifying the lowest and highest focal planes corresponding to the gel boundaries and multiplying the number of included slices by the voxel depth.

2.9.3 Quantification of hydrogel top-surface geometry

The top-surface geometry of PEGDA hydrogels was quantified from confocal fluorescence z-stacks using a custom Python-based analysis pipeline previously developed in the laboratory. For each stack, the axial position of maximum fluorescence intensity was identified at each (x,y) pixel, corresponding to the bead-coated top-surface of the gel. Subpixel accuracy along the z-axis was achieved by fitting a parabolic function to the intensity profile around the maximum.

A well-shaped Region Of Interest (ROI) was automatically segmented from the maximum-intensity projection and scaled to 90% of its original size to exclude peripheral artifacts associated with gel retraction. Height maps were converted from pixel units to micrometers using voxel metadata extracted from the image files.

To separate global and local surface features, height maps were decomposed into long-wavelength and short-wavelength components using sequential Gaussian filtering. A planar surface was fitted to the height data. Surface roughness was quantified from the

band-pass residuals, representing intermediate and short-scale topographical variations relevant for passive object positioning.

All metrics were computed exclusively within the valid ROI and applied uniformly across all samples to ensure quantitative comparability between UV exposure conditions.

2.9.4 Segmentation pipeline

To quantitatively evaluate substrate-dependent cell-adhesion, HT1080 human fibrosarcoma cells were used as a model system to test adhesion and seeded on glass and on 7.5% w/w PEGDA hydrogels. Confocal fluorescence microscopy was performed using Nikon CFI Plan Apo 20x objective (air-immersion, N.A. 0.75, WD 1 mm, catalog# MRD00205, Nikon) and Nikon CFI Plan Apo Lambda S 40XC Sil objective (oil-immersion, N.A. 1.25, WD 0.3 mm, catalog# MRD73400, Nikon). 20x datasets were analyzed using a minimal and fully automated image analysis pipeline implemented in Python.

Cell segmentation was performed using the Cellpose general segmentation model. ND2 images were loaded using the nd2 Python library and reshaped to a channel-first format to ensure compatibility with the segmentation model. The first two acquisition channels were used for segmentation to match the fluorescence signals employed for cell identification. Segmentation was executed using near-default parameters (batch_size = 32, flow_threshold = 0.4, cellprob_threshold = 0.0) combined with global intensity normalization, maintaining a deliberately minimal and reproducible workflow.

For quality control, the pipeline automatically generated side-by-side overlays of reference images and segmentation masks, along with compressed labelled mask files to enable rapid manual inspection. Morphological measurements were extracted from labelled masks using scikit-image regionprops_table, and cell area was computed in physical units (μm^2) using pixel calibration metadata embedded in the ND2 files. Single-cell area measurements were exported as CSV files and aggregated across experimental groups. Statistical summaries included per-image histogram, pooled distributions, and boxplots with overlaid single-cell measurements, enabling direct comparison of spreading behavior between substrates.

2.10 Nanoindentation measurements

Mechanical characterization was performed on PEGDA hydrogels (7.5% w/w) fabricated as flat patterns using a UV exposure dose of 10 mJ/mm^2. Following photopolymerization, gels were allowed to swell overnight in PBS buffer before measurements. Nanoindentation experiments were carried out using an Optics11 Life – Chiaro system equipped with an OP1550 interferometric displacement sensor and controlled via Piuma software. Measurements were conducted in Dulbecco's PBS (DPBS) without Ca^{2+} or Mg^{2+} (C-40232, PromoCell) to preserve hydrogel hydration and physiologically swelled state. The system integrates a piezoelectric actuator, an interferometric displacement readout, an inverted optical microscope for positioning, and a motorized XY stage for spatially resolved measurements. For each formulation, N = 2 independent hydrogels were analyzed.

Indentation experiments were performed using a spherical probe (colloidal probe) with a radius of 100 μm and a cantilever spring constant of 0.5 N/m. The relatively large probe radius was selected to average microscale heterogeneities within the hydrogel network while maintaining adequate spatial resolution for matrix-based mechanical mapping. Indentations were carried out up to an effective maximum indentation depth of approximately 5 μm. Given the probe radius, this corresponds to a δ/R ratio of approximately 0.05, ensuring that the small-deformation assumption underlying the Hertz contact model was satisfied. Indentation depth was further limited to minimize potential substrate effects, in accordance with standard nanoindentation guidelines for soft materials. Indentation was performed under displacement control at a constant loading rate of approximately 6 μm s^{-1}. Approach speed, indentation speed, and maximum indentation depth were kept constant across all measurements to ensure comparability between samples and experimental conditions.

Probe calibration was performed in liquid before measurements. Contact position was determined using automated surface detection and verified by displacement-controlled indentation test. Indentation was conducted under displacement control, and spatially resolved measurements were acquired as predefined grid-based matrix scans with automated surface detection at each point. Raw indentation data were exported from the tool-proprietary Piuma software as individual text files for each indentation point,

together with summary files reporting effective modulus values and spatial coordinates for matrix scans. A previously developed custom Python script was used to preprocess and reorganize these outputs into analysis-ready datasets. Loading, holding, and unloading phases were identified from the force-indentation curves based on slope changes in the displacement and force signals. Measurements lacking a clearly defined pre-contact region or exhibiting unstable baseline drift were excluded from further analysis. Data are reported as mean ± standard deviation.

2.11 Traction Force Microscopy (TFM)

Traction forces exerted by cardiac organoids on deformable PEGDA hydrogels were quantified using Traction Force Microscopy (TFM), implemented through a custom MATLAB pipeline developed by the Notbohm Research Group (University of Wisconsin-Madison)[13]. To simplify the quantification of 3D contractile behavior, the system was approximated as two-dimensional by restricting the analysis to bead displacements within a single imaging plane at the substrate–cardioid interface. This enables the application of standard 2D traction force microscopy (TFM).

A conventional post-detachment "stress-free" reference was not acquired. Instead, a pre-contraction frame (minimal deformation) was used as the reference image. Displacements were therefore computed relative to this reference, and traction outputs were interpreted as contraction-associated changes.

Time-lapse image stacks were first processed in Fiji (ImageJ) using the *Make Substack* tool to isolate the contraction window of interest. Raw acquisition was performed every 5 ms.

Substrate deformation was quantified by tracking fluorescent beads at the gel-glass interface. Fast Iterative Digital Image Correlation (FIDIC), within the above mentioned pipeline, was applied using a cumulative comparison approach, where each frame was compared to the pre-contraction reference image to compute two-dimensional displacement fields along the x- and y-directions (u and v). Displacement estimation is based on cross-correlation between pixel submatrices of the reference and deformed images. The method performs local image registration by scanning a kernel window across the image and maximizing similarity between corresponding regions in

consecutive frames. For each subset, correlation coefficients were integrated over the entire interrogation window to determine the most probable displacement vector.

Displacement was calculated on a regular grid defined by the subset size (w_0) and subset spacing (d_0), selected based on bead density and imaging resolution. In this work, a kernel size of 64 x 64 was selected, with a step size of 16 pixels between adjacent interrogation windows. These parameters represent standard values in 2D TFM and were selected to balance noise sensitivity and displacement accuracy. The resulting displacement fields, together with grid coordinates, were stored in MATLAB (.mat) files for subsequent traction reconstruction.

The MATLAB pipeline requires specification of spatial calibration (µm/pixel), Young's modulus (E), and Poisson's ratio (ν). Spatial calibration was obtained from microscope metadata and set to 2.7 x 10^{-7} m. Images were acquired using a Nikon CFI Plan Apo Lambda S 25x Sil objective (oil immersion, N.A. 1.05, WD 0.55 mm, catalog# MRD73250, Nikon). The Poisson's ratio was fixed at $\nu = 0.5$, consistent with the assumption of incompressible hydrogel behavior. Young's modulus values were derived from nanoindentation measurements and set to 5 kPa.

A binary domain mask was generated from corresponding transmitted-light images using a custom MATLAB script (find_boundary.m). Masks were generated as 8-bit images. This domain definition was used to restrict traction calculations to regions mechanically coupled to the organoid. Traction reconstruction was restricted to the region of effective mechanical coupling where beads remained in focus. This restriction minimizes artifacts from out-of-plane motion and optical defocusing inherent to the 2D approximation.

Traction force fields were reconstructed from the measured substrate displacements using Fourier Transform Traction Cytometry within the above mentioned MATLAB pipeline. To improve computational efficiency and numerical stability, Fourier Transform Traction Cytometry (FTTC) was introduced, allowing traction stresses to be calculated in Fourier space and reducing sensitivity to noise[36]. Subsequent developments incorporated optimized regularization strategies and Bayesian parameter selection to enhance robustness and reproducibility of traction reconstructions[37,38].

Calculations were performed using a regularized Fourier-based MATLAB implementation. Mechanical properties of the substrate, including Young's modulus,

Poisson's ratio, and spatial calibration, were specified in an external configuration file (ExperimentalSettings.txt) associated with each dataset. The algorithm therefore computes the inverse problem in Fourier space, applying Tikhonov regularization to stabilize the solution against noise amplification. Then it returned spatial maps of traction components (t_x, t_y) corresponding to contractile forces generated during organoid beating. The above mentioned dedicated MATLAB script was used to visualize displacement vectors and traction maps as color-coded fields for qualitative and quantitative assessment. TFM analysis produced MATLAB (.mat) files containing substrate displacement fields and traction force maps for each time point of the contraction cycle.

Given the 2D approximation, uncertainty in the reference configuration, and the variability in measured hydrogel stiffness, traction estimates should be interpreted as semi-quantitative. For traction reconstruction, a Young's modulus of E = 5 kPa, was used, corresponding to the median value obtained from nanoindentation measurements and representative of the compliant PEGDA formulation employed in TFM experiments.

3 Results

3.1 Ventricular cardiac organoids as self-organizing models of human cardiogenesis

This section of the results focuses on the reproducible generation of self-organized ventricular cardioids displaying chamber-like morphogenesis and synchronized contractile activity.

The most clinically relevant cardiac diseases predominantly affect the left ventricle, including myocardial infarction and both hypertrophic and dilated cardiomyopathies. Recent advances in stem-cell-derived cardiac organoid systems (cardioid) have enabled the generation of different human cardiac models, ranging from developmentally relevant heart organoids that recapitulate early fetal morphogenesis to chamber-specific constructs[14]. Ventricular cardioids provide a particularly suitable model for studying cardiac force generation due to their structural and functional resemblance to the force-producing compartment of the heart. Beyond its pathological relevance, the ventricle represents the primary force-generating chamber of the heart, operating under high-pressure mechanical loads.

For these reasons, ventricular cardioids provide a physiologically and clinically relevant model for investigating mechanisms of cardiac force generation. These models recapitulate key aspects of early human heart morphogenesis, including chamber-like cavity structure and synchronized contractile activity. Ventricular cardioids, therefore, provide experimentally tractable developmental systems that bridge the gap between 2D cardiomyocyte cultures and in vivo cardiac tissue. Ventricular cardioids emerge through intrinsic self-organization processes driven by signaling pathways that regulate cell differentiation. This developmental trajectory leads to the formation of chamber-like cavities, beating structures, and coherent electromechanical coupling[39]. Within this framework, generating reproducible ventricular cardioids is a critical prerequisite for mechanobiology studies aimed at quantifying force generation without disrupting organoid architecture.

3.1.1 Differentiation workflow and emergence of self-organized ventricular structures

We derived ventricular cardiac organoids from hiPSCs using a stepwise differentiation strategy that recapitulated early cardiac developmental signaling. On day -1, we seeded 5 x 10^4 hiPSCs per well in a 24-well plate, maintaining them in Essential 8 Flex Medium supplemented with ROCK inhibitor for 24 hours. We then induced cardiac differentiation through sequential modulation of developmental pathways controlling mesoderm specification and cardiomyocyte commitment. During the initial 2D phase, we started APS induction, promoting epithelial-mesenchymal transition and early mesodermal commitment. After 37 hours, we promoted the 3D transition, activated cardiac mesoderm differentiation, and refreshed the medium every 24 hours for four days while modulating the Wnt pathway[39]. This transition represented a key morphogenetic step, as it enabled multicellular compaction and spatial self-organization. In the final differentiation stage, we promoted cardiomyocyte specification, which we verified by the onset of spontaneous beating. Between day 2.5 and 4.5, organoids increased in size and formed chamber-like cavities (**Figure 6**), marking the transition from simple aggregated to structurally organized ventricular cardioids. Subsequent exposure to cardiomyocyte specification medium further supported differentiation and maturation, culminating in spontaneous beating between days 5.5 and 6.5 (**Figure 6**). Brightfield imaging (**Figure 6**, **A**) revealed a reproducible developmental trajectory across independent differentiations. Early cardioids appeared compact and spherical, whereas later time points revealed increased size, surface heterogeneity, and more pronounced chamber-like cavities. These structural features are consistent with progressive tissue remodeling during ventricular morphogenesis.

3.1.2 Functional maturation and quantitative characterization of cardioid growth

To quantitatively assess morphogenetic progression, we measured cardioid area across developmental time points. We performed area quantification on n = 24 independent cardioids tracked longitudinally across differentiation. We reported data as mean ± standard deviation (Mean ± SD, **Figure 6, B**). Cardioids displayed a monotonic increase in size from early aggregation to later maturation stages, indicating sustained tissue growth and structural stabilization. Cardioids preserved a globally spherical geometry throughout growth, indicating balanced tissue remodelling without structural collapse or fragmentation.

Relative area measurements showed a progressive fold-increase compared to early time points, reflecting coordinated proliferation rather than simple cell accumulation. When normalized to day 2.5, cardioids exhibited a steady increase in size, reaching approximately a 1.7-fold expansion by day 9.5. Absolute area values approached ~3.5 x 10^5 μm^2 at the final time point, confirming consistent volumetric growth across the population. This controlled growth was particularly relevant for subsequent mechanical experiments. Reproducible growth dynamics reduced inter-sample variability, improving experimental consistency, directly informed hydrogel fabrication design and enabling comparison of deformation-based measurements across conditions.

Then we performed functional validation through calcium imaging, providing a direct readout of excitation-contraction coupling and tissue synchronization. Fluorescence imaging revealed spatially homogeneous calcium activation across the organoid volume, indicating coordinated electrical propagation. Normalized calcium traces displayed periodic oscillations with consistent amplitude and inter-beat intervals. The presence of synchronized calcium activity across the entire cardioid establishes that the generated cardioids behave as multicellular tissues capable of producing coordinated activity.

The combination of structural self-organization, controlled growth, and synchronized calcium dynamics (**Figure 6, C**) demonstrates that we generated ventricular cardioids capable of acting as a robust biological platform for mechanical interrogation. Three aspects are particularly critical. First, the formation of cavities supporting ventricular-

like morphogenesis. Second, the preservation of spherical geometry enabling reproducible interaction with patterned hydrogel environments. Third, the emergence of synchronized contractile activity capable of generating measurable substrate deformation. Together, these characteristics ensure that the cardioids provide both biological relevance for integration with the PEGDA photopatterned platform.

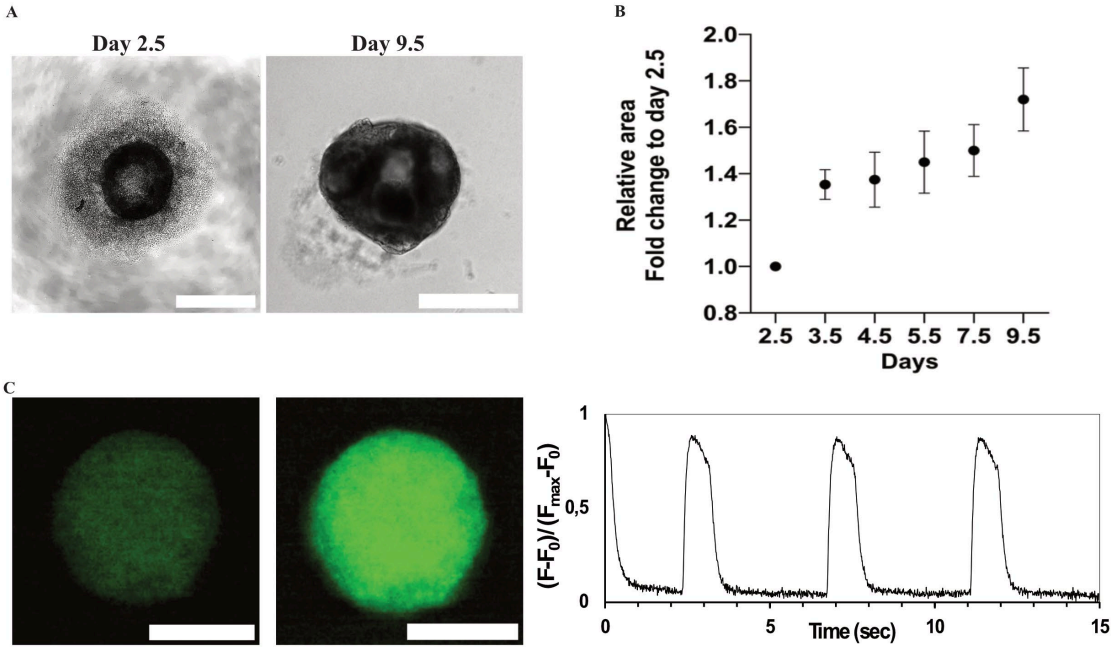

Figure 6: Ventricular cardiac organoid formation and functional maturation.

(A) Brightfield images illustrating ventricular cardioid development from early aggregation (day 2.5) to structurally mature cavity-containing organoids (day 9.5). Organoids exhibit increasing size, tissue compaction, and surface remodelling during morphogenesis; **(B)** quantitative analysis of projected organoid area normalized to day 2.5 demonstrates progressive growth and structural stabilization during differentiation. Data are reported as mean ± SD across independent organoids; **(C)** representative calcium imaging showing spatially coherent calcium activation across the tissue. Normalized fluorescence traces reveal periodic synchronized calcium transients indicative of coordinated excitation-contraction coupling and functional maturation.

3.2 Production and characterization of PEGDA gels

Mechanical force generation is a defining functional output of developing cardiac tissues, yet its quantification in three-dimensional human cardiac organoids remains limited by the lack of mechanically compliant and optically compatible support platforms. As outlined in the introduction, commonly used bioadhesive or stiff substrates can mechanically constrain organoids, alter their morphology, and interfere with functional readouts. To minimize these effects, cardioids must be hosted in thin, transparent, and intrinsically non-bioadhesive hydrogels that preserve tissue autonomy while remaining compatible with high-resolution imaging.

To address this objective, we adapted the LigHTS photopatterning workflow [9], originally developed for GelMA hydrogels, to PEGDA. PEGDA represents a cost-effective, modular, and intrinsically non-bioadhesive alternative that is, in principle, well suited for optical microscopy. However, because low-molecular weight PEGDA (575 Da) is not commonly used to generate imaging-grade hydrogels, its optical clarity, structural robustness, and compatibility with photopatterning could not be assumed and required systematic experimental validation.

To establish PEGDA as a viable material for imaging-compatible hydrogel supports, we adapted the LigHTS photopatterning workflow[9] and performed stepwise optimization of material composition, physical processing, and photochemical parameters. We first evaluated whether PEGDA could be reproducibly polymerized into homogeneous gels across a wide range of polymer concentrations, with particular attention to optical clarity and structural stability. Given the strong turbidity observed at intermediate PEGDA concentrations in preliminary trials, we next tested whether extended mixing, sterile filtration, and vacuum degassing could improve gel homogeneity and transparency without altering photochemistry.

Once an optically compatible PEGDA formulation was identified, we focused on controlling gel thickness through photochemical modulation. By systematically varying tartrazine concentration while keeping PEGDA and photoinitiator levels constant, we mapped the gelation window under different UV exposure doses.

Finally, we quantitatively characterized PEGDA gel height by confocal z-stack imaging to establish a predictive relationship between illumination parameters and final gel thickness within the range required to host 450-550 µm cardiac organoids. All fabrication, processing, and imaging procedures were performed as described in the Materials and Methods section.

3.2.1 PEGDA concentration is the primary determinant of optical clarity and structural stability

We first assessed whether PEGDA could be reproducibly polymerized into homogeneous and optically clear hydrogels using the LigHTS workflow [9]. We fabricated PEGDA hydrogels across a broad concentration range (3.75% w/w, 5% w/w, 7.5% w/w, 15% w/w, 30% w/w, 60% w/w, and 90% w/w) under identical photochemical conditions (**Figure 7** and **Supplementary Figure 1**). We tested four different UV doses: 6 mJ/mm^2, 9 mJ/mm^2, 12 mJ/mm^2, and 15 mJ/mm^2. We used only 25 mJ/mm^2 for 5% w/w PEGDA hydrogels.

Across these conditions, PEGDA concentration strongly influenced the hydrogel optical appearance. PEGDA gels at intermediate concentrations (15% w/w, 30% w/w, and 60% w/w) exhibited pronounced optical turbidity, which increased with UV dose (**Supplementary Figure 1**). Gels at 30% w/w PEGDA exhibited the strongest light scattering, appearing opaque immediately after polymerization. This opacity was associated with the formation of microdomains, consistent with phase separation occurring during polymer network formation. Similar microdomain formation was observed at 15% w/w and 60% w/w PEGDA, resulting in significant optical scattering and heterogeneous light transmission across the gel.

We detected phase separation also at 7.5% w/w PEGDA. However, this lower polymer concentration prevented significant optical scattering. So, 7.5% w/w PEGDA hydrogels remained optically clear and mechanically stable across all tested illumination conditions.

At the highest concentration tested (90% w/w), gels appeared comparatively clearer than those in the intermediate concentration range. However, these gels rapidly developed cracks and delaminated from the substrate (**Figure 7** and **Supplementary**

Figure 1). Delamination was particularly evident at 12 mJ/mm^2. This is consistent with stress accumulation during rapid crosslinking of highly concentrated low-molecular weight PEGDA.

Reducing PEGDA below 7.5% w/w revealed a lower bound for reliable gel formation. At 5% w/w, gelation occurred only at elevated UV doses (25 mJ/mm^2). By contrast, at 3.75% w/w, gelation did not occur under the tested photochemical conditions.

Together, these results identify PEGDA concentration as the main parameter governing optical clarity and mechanical properties. As shown in **Figure 7**, increasing UV dose does not rescue optical clarity at intermediate and high PEGDA concentrations, indicating that polymer concentration dominates gel transparency under these conditions. The complete dataset across all tested concentrations is reported in **Supplementary Figure 1**.

.

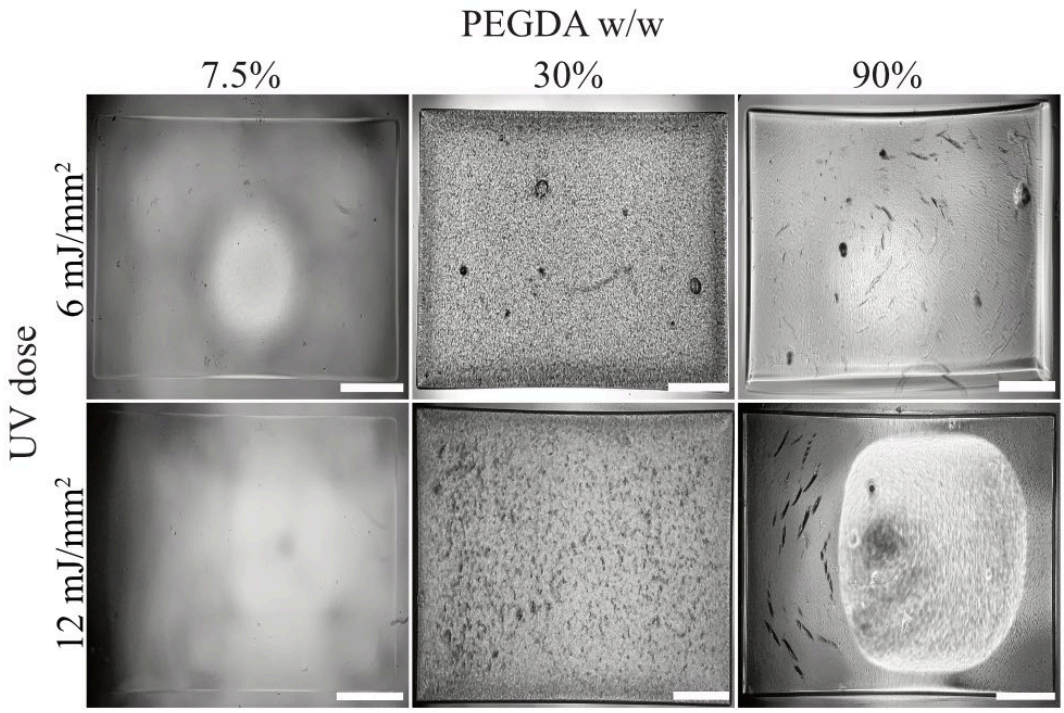

Figure 7: PEGDA concentration governs hydrogels optical clarity and mechanical properties.

Representative brightfield images of flat PEGDA hydrogels fabricated using the LigHTS photopatterning workflow at three representative PEGDA concentrations (7.5% w/w, 30% w/w and 90% w/w) and two UV exposure doses (6 mJ/mm2 and 12 mJ/mm2). Rows correspond to increasing UV dose, while columns report increasing PEGDA concentration. At intermediate PEGDA concentration (30% w/w), gels exhibit pronounced optical turbidity, associated with microdomain formation and phase separation. Phase separation is also detectable at 7.5% w/w PEGDA; however, the lower polymer fraction limits this effect. At the highest concentration tested 90% w/w, gels appear comparatively clearer but rapidly develop cracks and delaminate from the glass substrate. Additional PEGDA concentrations and UV dose conditions are reported in the Supplementary Figures. Scale bar: 500 μm.

3.2.2 Stirring and sterile filtering improve optical clarity at different PEGDA concentrations

We next tested whether physical processing of PEGDA precursor solutions influenced optical clarity. In particular, PEGDA solutions were stirred for 30 min and then sterile-filtered before casting, while maintaining standard photochemical conditions (**Supplementary Figure 2**).

Across all tested PEGDA concentrations, these processes influenced the hydrogel optical appearance. At 7.5% w/w PEGDA, gels prepared from only stirred precursor solutions were already optically transparent, but additional filtration resulted in further improvement in visual clarity and homogeneity across the patterned region. At 15% w/w PEGDA, filtration produced a marked improvement in optical transparency compared to stirred-only conditions, reducing visible micro-heterogeneities and improving overall brightfield image quality. In contrast, 30% w/w PEGDA hydrogels remained visibly opaque regardless of the filtration process.

Together, these results differ from what is reported in literature for PEGDA hydrogels, where increasing polymer concentration is often associated with improved optical transparency[40]. In our system, increasing PEGDA concentration resulted in progressively higher turbidity. This difference can be related to the low molecular weight of the PEGDA used in this study (575 Da). We hypothesized that the 7.5% w/w PEGDA concentration is low enough to provide clear gel even in the phase separation regime.

Collectively, our data indicates an intrinsic upper limit to optical transparency for low-molecular weight PEGDA. Based on these results, we selected 7.5% w/w PEGDA as the formulation providing the best balance between optical clarity and mechanical properties, and we therefore used it for all subsequent experiments.

3.2.3 Tartrazine concentration and UV dose define the PEGDA gelation window

Having identified the optimal PEGDA formulation, we next focused on controlling gel thickness through photochemical modulation. We systematically varied tartrazine concentration while maintaining PEGDA at 7.5% w/w and the photoinitiator concentration constant at 1 mg/mL. To achieve this objective, we fabricated flat patterned gels using PRIMO (Alvéole)-based photopatterning testing four different tartrazine concentration (1 mg/mL, 5 mg/mL, 10 mg/mL and 15 mg/mL) and UV doses (5 mJ/mm^2, 10 mJ/mm^2, 25 mJ/mm^2 and 50 mJ/mm^2, **Figure 8**).

At the lowest tartrazine concentration (1 mg/mL), gels formed reliably at low UV doses (5 mJ/mm^2 and 10 mJ/mm^2). While increasing the UV dose under these conditions led to stitching artifacts and irregular gel boundaries, indicative of overexposure. As tartrazine concentration increased, the UV dose required for stable gel formation shifted progressively toward higher values. At the highest tartrazine concentrations tested (15 mg/mL), gel formed only at high UV doses (25 mJ/mm^2 and 50 mJ/mm^2), while lower doses failed to induce complete crosslinking.

Collectively, these observations demonstrate that tartrazine acts as an effective photoabsorber, attenuating UV penetration and modulating polymerization depth.

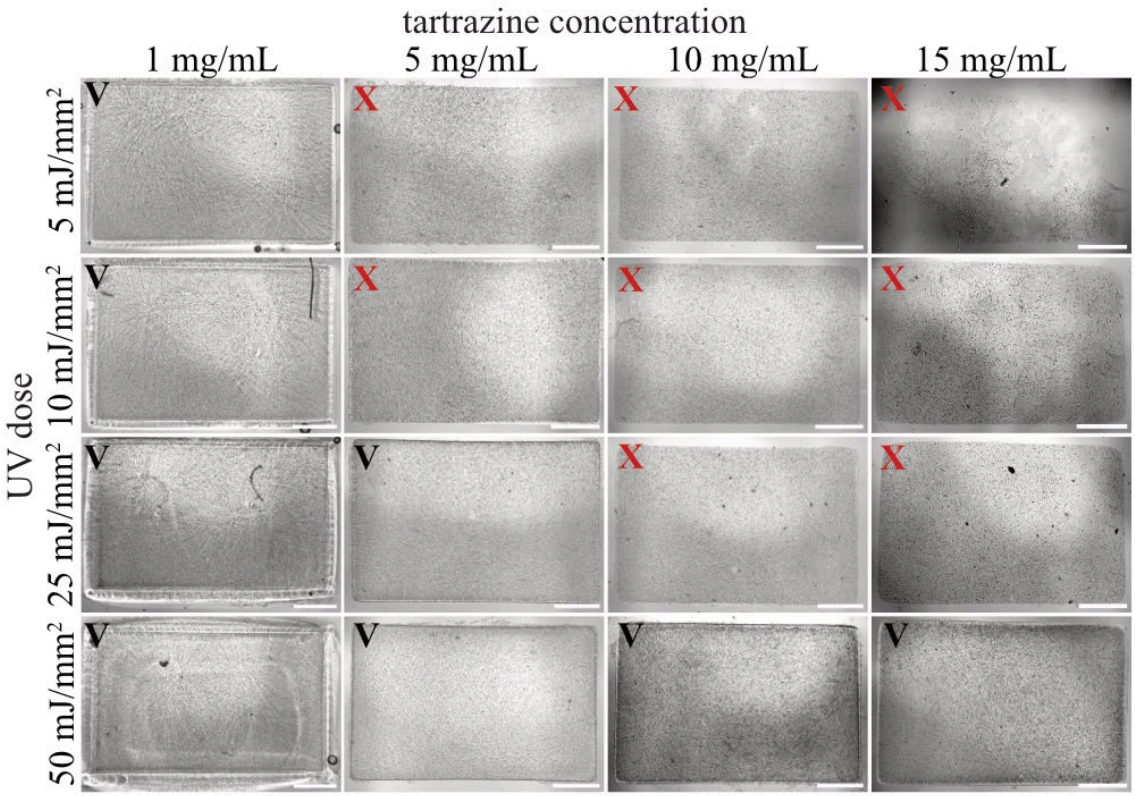

Figure 8: Combined effect of tartrazine concentration and UV dose on PEGDA hydrogel formation. Representative brightfield images of flat PEGDA hydrogels fabricated using PRIMO photopatterning across increasing tartrazine concentrations (1 mg/mL, 5 mg/mL, 10 mg/mL, and 15 mg/mL) and UV exposure dose (5 mJ/mm^2, 10 mJ/mm^2, 25 mJ/mm^2, and 50 mJ/mm^2). Each column corresponds to a fixed tartrazine concentration, while rows represent increasing UV dose. At the lowest tartrazine concentration (1 mg/mL), hydrogels show signs of overexposure and boundary irregularities at higher doses. Increasing tartrazine concentration progressively shifts the gelation window toward higher UV doses. At the highest tartrazine concentration (15 mg/mL), complete gel formation is restricted to high UV exposure doses. These results demonstrate that tartrazine acts as an effective photoabsorber, modulating light penetration and polymerization depth. Scale bars: 500 µm.

3.2.4 Quantitative confocal characterization defines cardioid-compatible PEGDA gel thickness

To establish a quantitative relation between UV exposure dose and PEGDA gel thickness, we tested five different UV doses (3 mJ/mm^2, 6 mJ/mm^2, 9 mJ/mm^2, 12 mJ/mm^2 and 15 mJ/mm^2 with four technical replicates per condition) with the optimal PEGDA solution for microscopy (7.5% w/w PEGDA, 1 mg/mL LAP and 1 mg/mL tartrazine).

We performed confocal z-stack imaging and analyzed gel thickness as described in section 2.9.2. We observed that gel thickness increased monotonically with UV dose, consistent with dose-dependent photo-crosslinking dynamics. We reported results as mean ± standard deviation. At the lowest exposure dose (3 mJ/mm^2), gels reached an average height of 321 ± 2.5 µm. Increasing the exposure to 6 mJ/mm^2 resulted in a marked increase in gel height to 487 ± 4.5 µm. Further increases in UV dose led to progressively thicker gels, with average thickness values of 609 ± 8 µm at 9 mJ/mm^2, 735 ± 12 µm at 12 mJ/mm^2, and 842 ± 19 µm at 15 mJ/mm^2.

We cross-checked these results with direct inspection of the z-stack. Based on this method, we obtained similar results. Gels fabricated at 3 mJ/mm^2 reached an average height of 332 ± 11 µm, 479 ± 10 µm at 6 mJ/mm^2, 610 ± 4.5 µm at 9 mJ/mm^2, 738.5 ± 13 µm at 12 mJ/mm^2, and 874 ± 15 µm at 15 mJ/mm^2. The quantitative distribution of individual measurements and the agreement between the thickness values from the macro-extracted projection and manual inspection of the raw data are reported in **Figure 9**. Beyond mean thickness values, the scatter distribution of individual measurements revealed a highly reproducible fabrication process. The close overlap between measurement methods further supports the robustness of the segmentation workflow and excludes systematic bias in thickness estimation.

Together, these measurements provide a quantitative framework for selecting illumination parameters based on the desired gel geometry. UV doses in the range of 9-15 mJ/mm^2 produced gel heights compatible with hosting 400-500 µm cardioids, whereas lower doses generated thinner gels that may be advantageous for applications requiring increased compliance or enhanced force transmission. Based on these

observations, 8 mJ/mm^2 was selected as an efficient working dose for subsequent experiments.

In summary, we adapted the LigHTS photopatterning workflow[9] to systematically produce PEGDA hydrogels that are thin, optically compatible, and non-bioadhesive to support 3D cardiac organoids. During these steps, PEGDA concentration emerged as the dominant determinant of optical clarity and structural stability. We determined that 7.5% w/w PEGDA was the only formulation consistently suitable for microscopy. We found that physical processing steps partially improved transparency at intermediate concentrations but failed at high polymer content. Within the optimized PEGDA regime, we determined tartrazine concentration and UV dose to achieve reproducible and quantitative control of gel thickness. We supported these results through confocal z-stack measurements, thereby establishing fabrication conditions compatible with cardioid housing.

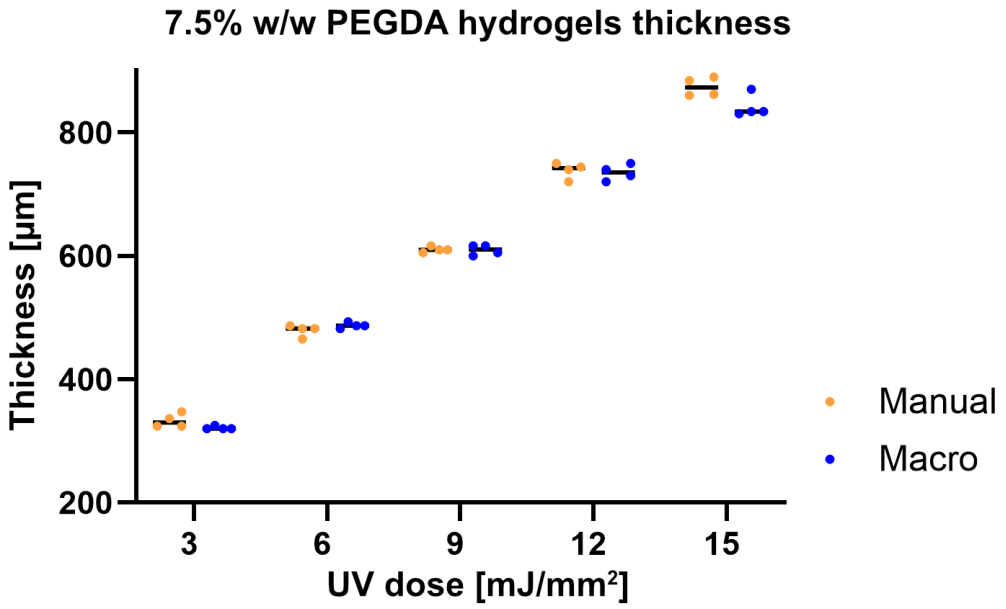

Figure 9: Quantitative control of PEGDA hydrogel thickness as a function of UV exposure dose. Scatter plot of confocal z-stack-derived thickness measurements for flat 7.5% w/w PEGDA hydrogels fabricated at increasing UV doses (3-15 mJ/mm^2). The graph presents the thickness values for each hydrogel characterized in two different ways: from the macro-extracted median projection (in blue) and from manual inspection of raw data (in orange). Gel thickness increases monotonically with exposure dose while maintaining low variability and strong agreement between quantification methods, demonstrating reproducible control of vertical polymerization depth.

3.2.5 Quantitative assessment of PEGDA non-bioadhesive behavior

To experimentally validate the non- bioadhesive properties of PEGDA hydrogels, we seeded HT1080 fibrosarcoma cells on flat glass substrates and on 7.5% w/w PEGDA gels under identical culture conditions. HT1080 fibrosarcoma cells were selected due to their highly adhesive and migratory phenotype, which makes them a sensitive model for detecting substrate-dependent differences in cell spreading. We performed a Proof-of-Concept (PoC) experiment comparing cell morphology and spreading on glass and on 7.5% w/w PEGDA hydrogels. To validate this experiment, we acquired representative fluorescence images at both 20x and 40x objective. This analysis revealed a clear morphological transition between substrates. Cells cultured on glass displayed pronounced spreading, elongated morphology, and the formation of protrusive structures consistent with strong substrate adhesion. In contrast, cells seeded on PEGDA hydrogels remained predominantly rounded, exhibited limited protrusive activity, and showed reduced surface contact area.

To objectively quantify this effect, we applied a minimal segmentation pipeline to extract single-cell morphological measurements. Automated segmentation and subsequent area quantification revealed a substantial reduction in cell spreading on PEGDA compared to glass (**Figure 10**).

These findings provide quantitative evidence of the non-bioadhesive behavior of PEGDA hydrogels. The inability of cells to establish strong adhesive contacts confirms that PEGDA minimizes cell-matrix anchoring, thereby preventing substrate-induced morphological bias. This characteristic is particularly important for self-organizing cardiac organoids, where excessive adhesion may disrupt tissue integrity, alter morphogenesis, or induce partial disaggregation in embedded organoids. Consequently, PEGDA represents a mechanically permissive yet bioinert support suitable for preserving organoid architecture while enabling downstream mechanical readouts.

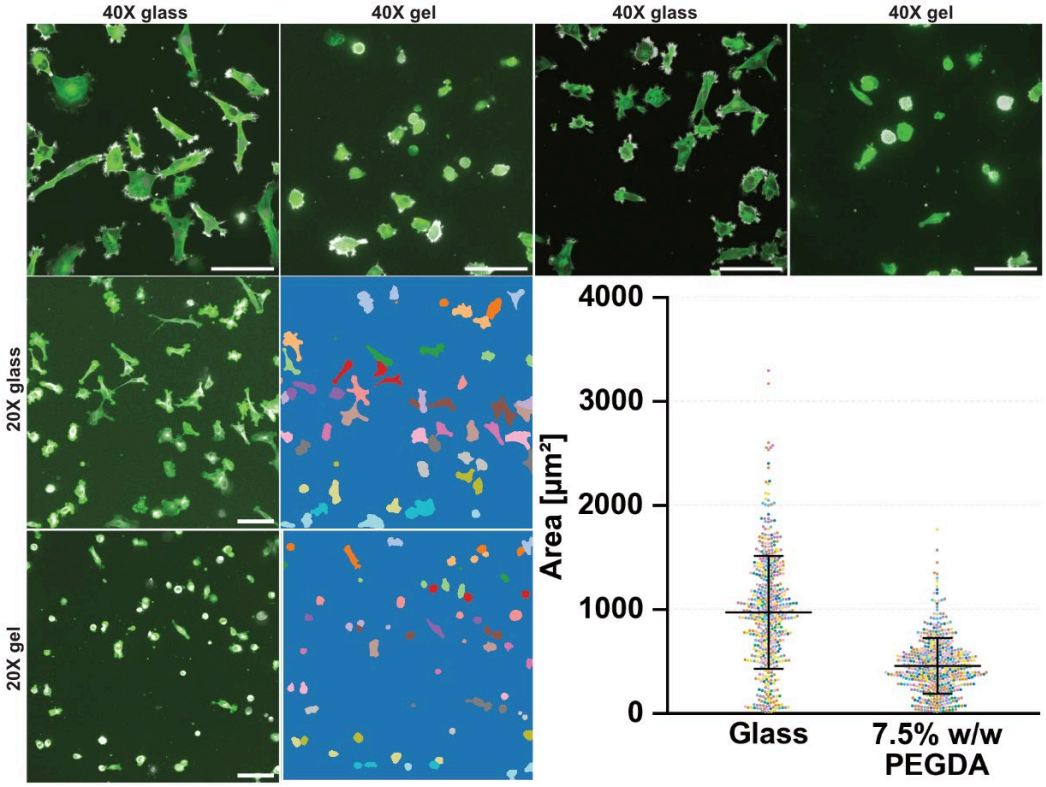

Figure 10: Quantitative assessment of PEGDA non-bioadhesive behavior using HT1080 cell seeding.

Representative fluorescence images of HT1080 fibrosarcoma cells cultured on glass and on 7.5% w/w PEGDA hydrogels acquired at 40x and 20x magnification. Cells on glass exhibit pronounced spreading, elongated morphology, and formation of adhesive protrusions, whereas cells on PEGDA remain rounded with minimal substrate interaction. Segmentation masks generated using a Cellpose-based analysis pipeline enabled automated extraction of single-cell areas from calibrated ND2 images. Quantitative analysis (right) shows a significant reduction in projected cell area on PEGDA compared to glass, confirming the non-bioadhesive behavior of the hydrogel and supporting its suitability as a mechanically permissive platform for self-organizing cardiac organoids.

3.2.6 Nanoindentation confirms cardioid-compatible mechanical compliance of 7.5% w/w PEGDA hydrogels

Finally, we quantified the mechanical response of 7.5% w/w PEGDA hydrogels through nanoindentation measurements performed under fully hydrated conditions. The indentation protocol consisted of sequential loading, hold, and unloading phases, allowing us to characterize both elastic stiffness and time-dependent relaxation behavior of the polymer network (**Figure 11** , **A-B**).

The loading curves showed a smooth and reproducible increase in indentation depth across replicates (**Figure 11**, **A**), indicating homogeneous network formation and consistent crosslinking density throughout the gel. During the hold phase, the load exhibited a modest time-dependent decrease (**Figure 11**, **B**), revealing fluid redistribution within the hydrogel matrix and confirming the presence of poroelastic relaxation mechanisms typical of hydrated PEG networks. Unloading curves demonstrated substantial recovery of the imposed deformation, with minimal residual indentation (**Figure 11**), indicating that the hydrogel response remained predominantly elastic within the explored deformation regime. The low dispersion observed between replicate curves further supports the mechanical uniformity of the fabricated gels and confirms the robustness of the photopolymerization protocol. From a quantitative perspective, the measured deformation under applied loads places the PEGDA formulation within the soft, tissue-relevant mechanical regime required for cardiac mechanobiology applications. In particular, the observed compliance ensures that the substrate can undergo measurable deformation under cardioid-generated contractile forces while preserving sufficient mechanical stability.

Together with optical and geometric characterization, these nanoindentation results support the selection of this formulation for subsequent cardioid housing and mechanobiology experiments.

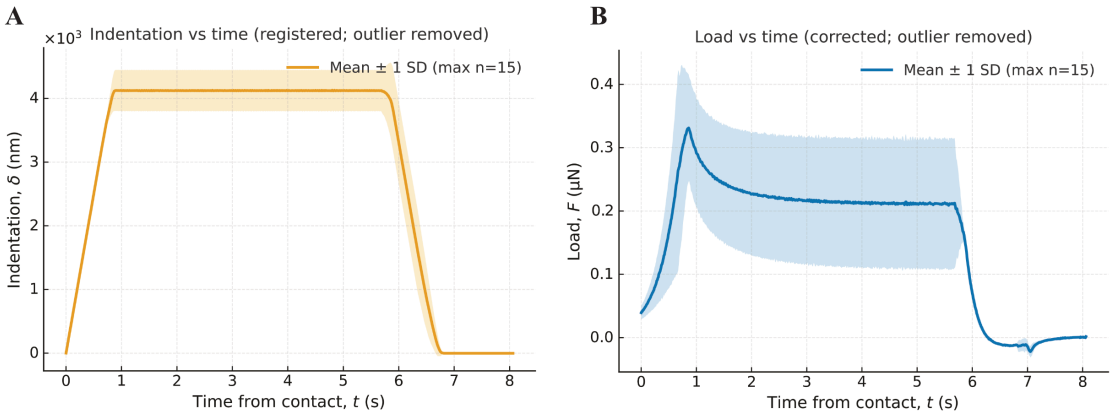

Figure 11: Nanoindentation mechanical characterization of 7.5% w/w PEGDA hydrogels.

(A) Mean indentation depth versus time showing the loading, hold, and unloading phases, with limited variability across replicates (mean ± SD). The stable plateau during the hold phase indicates controlled indentation under constant deformation; n represents 15 of the 16 measurements in matrix scan array on the same gel; **(B)** Corresponding load-time response highlighting an initial force peak followed by relaxation during the hold phase, consistent with poroelastic redistribution within the hydrated PEGDA network and partial recovery upon unloading.

3.3 Cardioid seeding and functional coupling on patterned PEGDA hydrogels

In this final result section, we demonstrate that PEGDA hydrogels patterned via grayscale-controlled photopolymerization can be engineered to host and position human cardiac organoids (cardioids). An initial housing design confirmed the feasibility of passive cardioid positioning but required high UV doses that compromised gel quality. A second, optimized design iteration yielded reproducible, optically clean cavities that improved seeding efficiency at lower UV doses. Together, these results establish PEGDA-based patterned hydrogels as a mechanically permissive and modular platform for controlled cardioid placement, forming the basis for downstream force-related measurements.

In the previous chapter, we established the fabrication parameters for producing PEGDA hydrogels with optical compatibility characteristics, and mechanical properties compatible with biological applications. However, material optimization alone does not guarantee functional performance. The critical next step was to demonstrate that these hydrogels can be engineered to achieve reproducible positioning of cardioids in a passive high-throughput fashion, while maintaining the high-resolution imaging properties required for functional analysis with Traction Force Microscopy.
In fact, force generation is a central functional output of cardiac tissue development and maturation, yet remains difficult to quantify in three-dimensional cardiac organoids due to the lack of mechanically permissive and imaging-compatible support systems.
To this end, we focused on the formulation identified as the most promising in Chapter 4: 7.5% w/w PEGDA containing 1 mg/mL LAP. We also lowered the tartrazine concentration to 1 mg/mL to reduce light attenuation during photopatterning, thus enabling the fabrication of deeper topographical features necessary to confine 3D cellular aggregates, without requiring excessive UV exposure time.

3.3.1 First housing design: fabrication limits and inefficient cardioids seeding

We first evaluated a housing design based on a two-level dose modulation (one for the top and one for the bottom of the cavity). This experiment was intentionally exploratory in terms of design complexity. The primary aim was to estimate the hydrogel thickness in the bottom of the cavities and in the gel surrounding them, and to evaluate the effectiveness of cardioid positioning during seeding.

We patterned gels using the PRIMO maskless photopatterning system with a 4x objective. We designed a geometry consisting of cavity-like features intended to act as slots for cardioids. We generated three-dimensional topography using a nine-level grayscale modulation ranging from 10% to 90% of the nominal UV dose, applied in 10% increments. We chose this approach to create a stepped cavity profile to guide organoid seeding. For this first design, we tested four nominal UV exposure doses: 5 mJ/mm^2, 10 mJ/mm^2, 25 mJ/mm^2, and 50 mJ/mm^2 with three technical replicates for each dose. To assess the fabricated structures, we performed confocal z-stack imaging using fluorescent beads deposited at the gel-glass interface. We generated three-dimensional reconstructions and depth colormaps from these z-stacks, enabling direct visualization of cavity depth, slope, and uniformity across the patterned region.

Grayscale-controlled photopolymerization generated cavity-like features at all tested doses. However, at the lowest nominal exposure, the resulting cavities were shallow with limited vertical relief between the gel surface and the cavity bottom (around 300 µm), compared to the average diameter of the organoids. Depth colormaps and 3D reconstructions revealed that these structures were insufficient to fully contain a cardioid and, therefore, unlikely to promote stable positioning. Increasing the nominal dose to 25 mJ/mm^2 and 50 mJ/mm^2 led to a marked increase in cavity depth, confirming that reduced tartrazine concentration effectively expanded the gelation window and enabled thicker gels (600-900 µm). We obtained the deepest slots at 50 mJ/mm^2, with vertical dimensions approaching those required to host a cardioid. However, this increase in depth was accompanied by fabrication issues. At this higher dose, gels exhibited pronounced stitching effects that could hinder high-resolution imaging. Thus, while the first design demonstrated that PEGDA can be patterned into deep, three-

dimensional housings, it also revealed a trade-off between cavity depth and gel quality when depth is achieved by increasing UV dose.

To quantitatively support these observations, we systematically characterized the top-surface geometry of the patterned gels by reconstructing the gel height via a dedicated Python script previously developed in the lab (**Figure 12** and **Supplementary Figure 3**). For each condition, the algorithm reconstructed the axial position of the gel top surface on a pixel-by-pixel basis by identifying the Z-location of maximum fluorescence intensity of the bead layer. We restricted the analysis to the central 90% of the well area to exclude peripheral artifacts arising from gel retraction. At the lowest UV dose (5 mJ/mm^2), reconstructed top-surface height maps showed limited thickness modulation and relatively smooth profiles, with surface variations dominated by the intended grayscale pattern. However, we observed visible stitching defects across the patterned region, indicating non-uniform polymerization over the illumination field. As the UV dose increased to 10 mJ/mm^2 and 25 mJ/mm^2, both the absolute height and spatial heterogeneity of the top surface increased. Height maps revealed pronounced ridge-like features at pattern transitions, indicating progressive loss of planar uniformity. At the highest UV dose tested (50 mJ/mm^2), surface reconstruction showed localized irregularities consistent with over-polymerization.

To test functional compatibility, we seeded cardioids onto the patterned gels. Before seeding, we sterilized gels incubating them in Primocin (1:500) overnight to prevent microbial contamination prior to cardioid deposition.

Immediately after casting via pipetting, cardioids remained on the gel surface and did not spontaneously enter the cavities. To promote passive settling in the gel cavities, we transferred the plate to the incubator and placed it on an orbital shaker at 20 RPM overnight.

Following agitation, cardioids seeded on gels fabricated at 50 mJ/mm^2 were consistently found within the deepest housing structures. Brightfield images confirmed that these cavities were capable of capturing and retaining cardioids once sufficient depth was achieved. In contrast, cardioids remained partially or fully outside the cavities on the hydrogels fabricated at 5 mJ/mm^2, 10 $mJ/mm^{2,}$ and 25 mJ/mm^2. Representative brightfield images illustrating these seeding outcomes across UV doses are shown in **Supplementary Figure 4**.

Despite the successful cardioids positioning for the 50 mJ/mm^2 condition, the associated stitching artifacts, degraded gel quality, and long-printing time made gels patterned with this UV dose unsuitable for the application.

In summary, the first exploratory campaign in slot design and fabrication suggested that cavity depth superior to the cardioid diameter were important for stable positioning. However, it also indicated that long exposures (50 mJ/mm^2) should be avoided to maintain high-resolution compatibility.

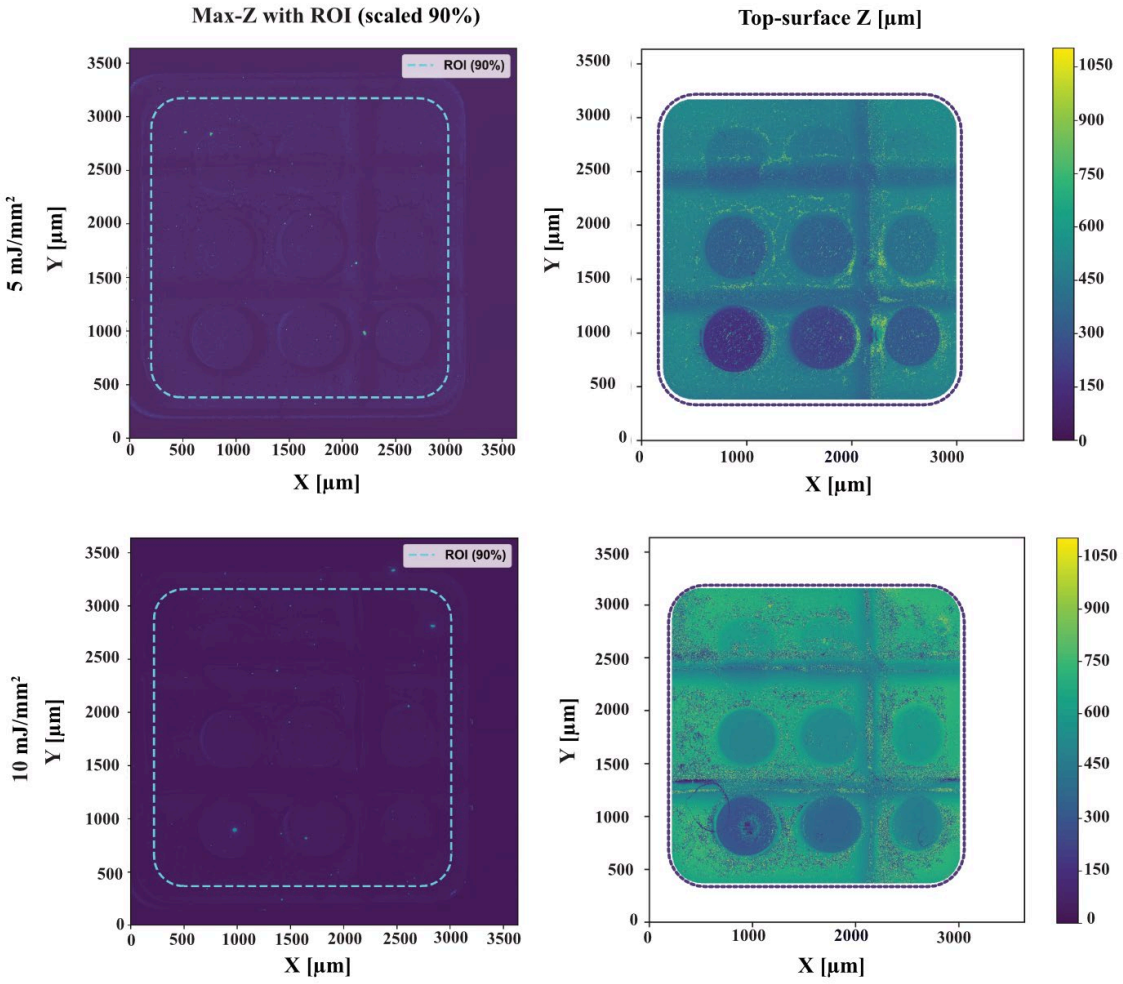

Figure 12: quantitative characterization of top-surface geometry in the first PEGDA housing design at 5 mJ/mm^2 and 10 mJ/mm^2 UV exposure dose.

Maximum-intensity Z projections (left) display the patterned region with the selection of the Region Of Interest (ROI) indicated by the dashed contour. Corresponding top-surface height maps (right) were obtained by extracting for each (x,y) coordinate the axial position of maximum fluorescence intensity of the bead layer at the gel-glass interface. The reconstructions reveal the progressive increase in cavity depth with UV dose, together with the emergence of spatial heterogeneities associated with grayscale photopolymerization.

3.3.2 Design optimization improved cardioid seeding

To overcome the limitations observed in the exploratory campaign, we designed a second geometry of slot structures. The primary goal was to improve the entry profiles of the slots, ensuring that cardioids would slide into the cavities even when fabricated at lower UV doses.

We replaced the sharp transition between cavity tops and bottoms with a funnel-like entry that guided cardioids into the cavities by grayscale dose transition between the two-levels (**Figure 13**, **A**). We generated three design variants with cavity bottom diameters of 450 µm, 500 µm, and 550 µm, comparable to the average cardioid size. We also increased the density of cavities to minimize the probability of organoids resting on the gel surface. We fabricated hydrogels using the same chemical formulation described in the previous chapter. Based on the test of UV doses reported in paragraph 3.2.4, and performed patterning at two maximum UV doses (8 mJ/mm^2 and 15 mJ/mm^2, **Supplementary Figure 8**) which we modulated according to the grayscale design. Preliminary optical inspection confirmed that these exposure settings yielded structures with excellent contrast and no visible stitching artifacts.

To quantitatively evaluate the morphological fidelity of this new design, we reconstructed the three-dimensional cavity surface from confocal z-stack acquisitions (**Figure 13, A; Supplementary Figure 5** ; **Supplementary Figure 6** ; **Supplementary Figure 7**). Fluorescent beads distributed across the gel provided an optical reference for surface localization during acquisition. For each stack, the axial coordinate corresponding to maximum fluorescence intensity was extracted at every (x,y) position, yielding a continuous height map of the cavity surface. Surface reconstruction revealed that the gradient design successfully produced a more funnel structure compared to the two-level design used in the exploratory campaign. However, residual geometric heterogeneities remained dose-dependent. Increasing UV exposure enhanced cavity depth but introduced stitching artifacts. Cavities with a nominal diameter of 450 µm displayed limited entry cross-section (**Supplementary Figure 7**), which could hinder organoid deposition. In contrast, the 500 µm and 550 µm designs exhibited improved radial symmetry and smoother entry slopes, consistent with reduced barriers for organoid seeding (**Supplementary Figure 5** ; **Supplementary Figure 6**).

Collectively, quantitative surface reconstruction demonstrates that the mechanical performance of the redesigned housing depends not only on nominal depth but also on geometric symmetry. These findings establish the geometric constraints that govern cardioid seeding and provide the quantitative basis for interpreting the functional results described below.

We seeded cardioids without orbital shaking leveraging the updated design with denser cavities and funnel-like entry for cardioid positioning. The gradient geometry significantly enhanced passive positioning efficiency. Cardioids successfully settled into cavities with nominal diameters of 500 µm and 550 µm, achieving near-complete enclosure (**Figure 13** , **B-C**). Confocal z-stack 3D reconstructions confirmed that in these conditions, the organoids were not resting on the gel top-surface, but were well seated within the engineered cavities (**Figure 13**, **C**).

In contrast, in the smallest cavities with a nominal diameter of 450 µm, the organoids remained physically confined above the slot entrance (**Supplementary Figure 8)**. Based on these observations, the 450 µm design was excluded from further characterization, and we restricted all subsequent analyses to the other two designs.

Collectively, these results demonstrate that PEGDA hydrogels patterned via grayscale photopolymerization can be engineered to passively position human cardiac organoids in a controlled and reproducible manner. This optimized platform provides a critical foundation for the subsequent analysis of cardioid-induced hydrogel deformation with TFM.

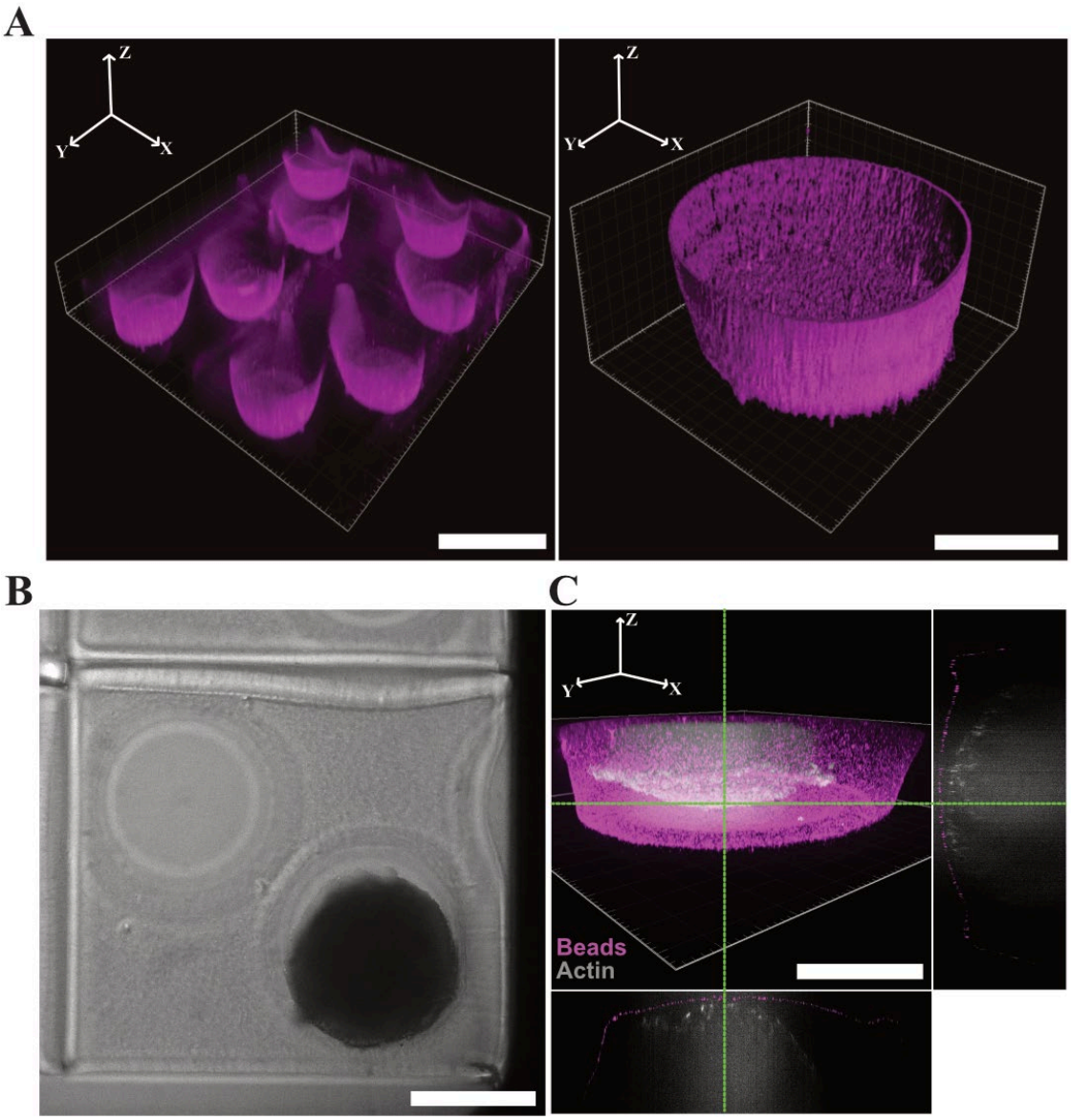

Figure 13: Gradient cavity design enables passive and stable cardioid housing in PEGDA hydrogels.

(A) Representative 3D confocal reconstructions of grayscale-patterned PEGDA cavities showing the funnel-like geometry generated by the optimized photopatterning workflow and the corresponding single-cavity reconstruction highlighting vertical confinement and continuous entry profile; (B) brightfield image illustrating successful passive positioning of a cardioid within the patterned cavity after static seeding; (C) orthogonal confocal sections showing the spatial relationship between fluorescent beads at the gel-glass interface and the actin-labelled cardioid, confirming that the organoid is deeply seated within the funnel rather than resting on the top surface. Scale bar: 500 µm.

3.3.3 Traction Force Microscopy (TFM)

As we discussed previously, an unresolved limitation in human cardiac organoids is that quantitative force measurements are rarely implemented. The force quantification becomes challenging in three-dimensional systems where optical accessibility, boundary conditions, and material behavior complicate both experimental acquisition and inverse reconstruction. 3D traction measurements require more complex experimental designs and modelling assumptions than standard 2D approaches. This makes them difficult to deploy in 3D biological models[34,41].

To study the force generated by cardioids, we imaged how cardioids adhering on the bottom of the gel cavities deformed the bead-coated substrate in a simplified 2D traction measurement configuration. The cardioid-matrix mechanical interaction was approximated as being dominated by a single compliant plane at the cavity bottom gel interface, where the organoid establishes contact. The present experiments represent a Proof-of-Concept (PoC) with limited sampling (n = 1). The resulting traction estimates should therefore be considered as a semi-quantitative measurement, and further studies with larger sample sizes will be necessary to address biological variability. Under these conditions, we used a standard 2D TFM workflow to reconstruct the traction field associated with organoid contraction. We interpreted the resulting traction as the planar projection of the full 3D load transfer.

A fundamental premise for solving the inverse elastic problem is the use of mechanically grounded inputs. Consequently, the TFM readout was paired with independent substrate characterization via nanoindentation (**Figure 14**, **A-B**). We measured stiffness values on the same material regime used in the experiments.

Figure 14-A reports the distribution of Young's modulus (E) values obtained by nanoindentation on PEGDA gels. Thickness values match the physiological cardiac range, with a central tendency dominated by the 4-6 kPa range, resulting in a median of ~5 kPa and a mean of ~6.25 kPa. This confirms that the substrate provides sufficient compliance to transduce contractile loads into measurable displacements. **Figure 14-B** illustrates the spatial distribution of stiffness, showing moderate heterogeneity (within a 3-10 kPa interval). This analysis motivates the choice of experimental setting used for mechanical readout.

We then analyzed calcium transients (**Supplementary Figure 9**, **B**) to ensure that the PEGDA support acts as a passive scaffold rather than a perturbing boundary condition. The traces show regular transients with stable peak morphology. Calcium transients occurred at a mean frequency of 0.7 ± 0.1 Hz (mean ± within-sample beat-to-beat variability, five beats from n = 1 cardioid). A stable beating frequency indicates that the chosen compliance regime preserves excitation-contraction coupling, validating the platform's biocompatibility and physiological relevance.

The operational principle of TFM relies on the ability to indirectly infer contractile forces from the deformation induced on an elastic substrate of known stiffness. Experimentally, this process requires the acquisition of a distinct pair of optical configurations at the cardioid-gel interface, where fluorescent beads are identified as deformation markers (**Figure 14-C** and **Supplementary Figure 9**, **A**). The first configuration is the reference state, acquired before the cardioid's contraction. The second, is the contracted state that captures the beads position during cardioid contraction. To quantify the transition between these states, we applied the FIDIC (Fast Iterative Digital Image Correlation) algorithm. Given the intrinsically three-dimensional geometry of the system and the concave cavity shape, not all regions of the gel remain simultaneously in optimal focus throughout contraction. For this reason, we restricted the displacement analysis to the region where beads remained sharply resolved, and mechanical coupling between cardioid and gel was visually evident. This restriction ensures that the reconstructed field reflects in-plane deformation rather than artifacts introduced by optical defocusing or out-of-plane motion.

The displacement vectors are visualized in **Figure 14-D.** The vector map reveals a spatially coherent contraction pattern, characterized by inward-directed vectors converging toward the contraction centre. The magnitude colormap indicates peak displacement values reach approximately 2-2.6 μm, as indicated by the displacement magnitude colorbar. The observed pattern is therefore attributable to substrate deformation induced by organoid contraction. Following displacement reconstruction, traction stresses were computed via the Fourier Transform using the experimentally measured Young's modulus as input. The resulting traction magnitude map (**Figure 14-E**) shows a heterogeneous but spatially organized stress distribution. Peak traction stresses reach approximately 400-550 Pa in localized regions. The stress field is not

uniformly distributed: high-stress regions are localized within the contraction area, while peripheral areas remain below approximately 50-100 Pa. The confinement of the stress field to the same spatial domain identified in the displacement map confirms the internal consistency of the inversion process. **Figure 14-F** reports the corresponding strain magnitude. Local strain values reach up to approximately 12-18% in the most deformed regions, while the majority of the active area remains within approximately 3-8%. Although these strains exceeded the infinitesimal limit typically assumed in linear elasticity theory, deformation remained fully reversible across contraction cycles.

Taken together, these results demonstrate that cardioid contraction generates a spatially coherent, mechanically localized deformation on the PEGDA substrate. The restriction of the analysis to the optically resolved bottom plane ensures that the reported tractions correspond to the mechanically coupled interface. The vertical components and full 3D stress transmission are not captured within this planar approximation.

In conclusion, **Figure 14** provides a materials-grounded PoC that the micropatterned PEGDA platform enables reliable quantification of cardioid contractile mechanics. With a substrate stiffness experimentally constrained at ~5 kPa, the system captures coherent displacement fields. This characterization confirms the platform's utility as a robust tool for the functional screening of 3D human cardiac models.

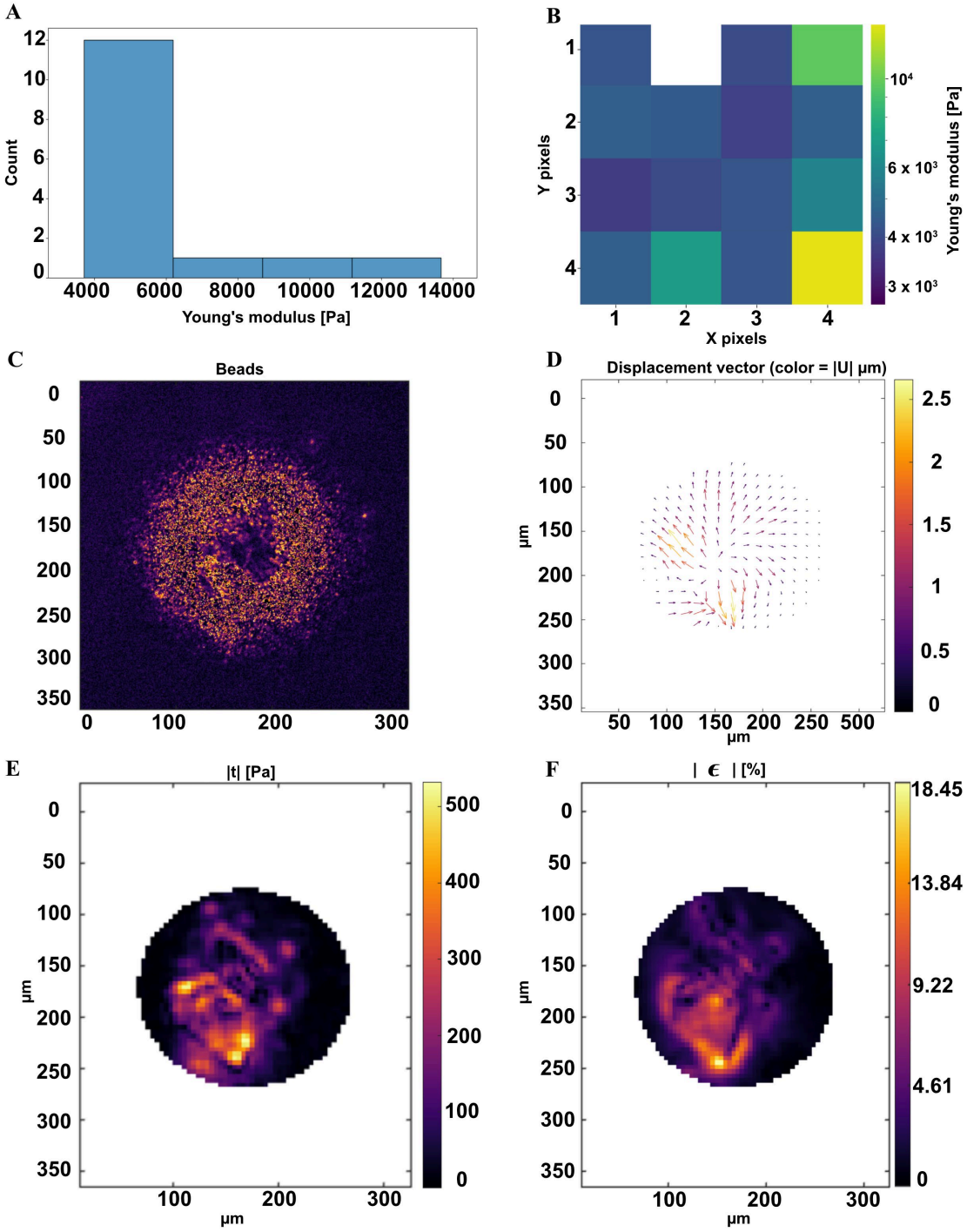

Figure 14: Traction force reconstruction during cardioid contraction.

(A-B) Young's modulus distribution of PEGDA hydrogels measured by nanoindentation; **(C)** fluorescent beads at the gel-cardioid interface used for displacement tracking; **(D)** In-plane displacement vectors between relaxed frame and contracted states, color-coded by magnitude; **(E)** traction stress magnitude (|t|, Pa) reconstructed by Fourier Transform; **(F)** corresponding in-plane strain magnitude (|e|,%).

4 Conclusions

4.1 Discussion of presented results

The present work addressed the lack of a dedicated platform for the functional characterization of human cardiac organoids. We developed a micropatterned PEGDA hydrogel platform enabling passive confinement and displacement-based mechanical readouts.

Together, the results demonstrate that grayscale UV photopatterning of PEGDA enables the fabrication of microcavities capable of hosting beating cardioids while preserving imaging accessibility. A central outcome is the identification of PEGDA as an effective compromise between structural stability, optical clarity, and fit for the biological system. In particular, the intrinsically non-bioadhesive nature of PEGDA prevented adhesion-driven spreading and preserved cardioid structural integrity, representing a meaningful deviation from commonly used bioadhesive matrices (e.g. GelMA). The optimization of polymer formulation and photopatterning parameters enabled the generation of cavities compatible with high-resolution imaging. Grayscale photopatterning provided vertical control of hydrogel geometry, allowing independent tuning of cavity depth and bottom thickness. This configuration ensured sufficient passive confinement to localize organoids while maintaining a mechanically compliant layer capable of transducing contraction into measurable substrate deformation.

Within this framework, the Proof-of-Concept implementation of TFM constitutes a key outcome. The observation of detectable bead displacement induced by cardioid beating confirms the feasibility of integrating organoids with substrate deformation. The proposed configuration can therefore be interpreted as an intermediate architecture between classical 2D TFM and fully embedded 3D traction measurements.

Furthermore, the entire fabrication and experimental workflow was implemented directly on standard 384-well plate, highlighting the intrinsic scalability of the platform. This supports integration into high-throughput experimental pipelines and enables parallel investigation of organoid mechanobiology across large experimental conditions.

4.2 Open technical challenges and additional insights

This thesis work identified the following limitations to this PoC. First, displacement acquisition within a single focal plane restricts traction estimation to in-plane components, while out-of-plane deformation remains unresolved. Given the intrinsically three-dimensional nature of cardioid contraction, this limitation may lead to incomplete characterization of force transmission and potential underestimation of total mechanical output.

Second, the thin deformable layer introduces sampling constraints governed by spatial Nyquist considerations. The combination of bead density, imaging resolution, and deformation amplitude defines a lower bound on detectable displacement, potentially leading to underestimation of small or rapidly varying mechanical events.

Temporal resolution also represents a critical constraint. Calcium transients underlying cardiomyocyte excitation-contraction coupling occur on the order of milliseconds, with rapid upstroke and decay phases. 3D TFM approaches represent a powerful tool for reconstructing volumetric force fields, their application is typically optimized for slower cellular processes. In these implementations, volumetric acquisition requires sequential scanning of multiple z-planes, often resulting in effective sampling rates on the order of one plane per second. This creates a fundamental mismatch between the millisecond-scale dynamics of cardioid contraction and the slower volumetric acquisition rate, leading to temporal undersampling of deformation, potential attenuation of displacement, and inaccuracies in rapidly evolving force fields. Moreover, this pipeline requires an increase in time exposure, which leads to phototoxicity effects. Within this context, planar imaging was a deliberate experimental choice. Achieving higher dimensional fidelity and more complete traction reconstruction inherently requires experimental compromises such as increased phototoxicity, temporal undersampling and greater acquisition and analysis complexity.

4.3 Outlook

Future developments may address the identified limitations through the integration of volumetric and low-phototoxic imaging strategies. Light-sheet microscopy represents a promising direction to enable three-dimensional displacement reconstruction while minimizing photobleaching and phototoxicity effects. Integrating light-sheet-based volumetric imaging could provide a powerful method to capture fully three-dimensional, time-resolved mechanobiology readouts while preserving physiological beating dynamics.

From a material perspective, future optimization may explore PEGDA formulations with different molecular weights to expand the mechanical and structural tunability of the platform. In this work, we selected a low-molecular weight PEGDA due to its availability for purchase during the thesis timeframe. However, higher-molecular weight PEGDA variants potentially enable greater deformation sensitivity. Systematic comparison across molecular weights could therefore provide additional control over stiffness and force transduction efficiency while preserving optical compatibility.

Overall, this work establishes a reproducible and scalable platform for passive positioning of cardioids compatible with substrate deformation analysis and correlation with traction force readout. The availability of structurally relevant three-dimensional cardiac organoids combined with quantitative force measurement represents a critical step toward physiologically meaningful in vitro disease modelling. The proposed platform provides a foundation for investigating pathological contractile phenotypes and advances the integration of organoid biology with quantitative cardiac mechanobiology. In this perspective, these approaches illustrate the potential of 3D cardiac models integrated within a PEGDA platform to bridge the gap between conventional standardized models for pharmaceutical research and translational applications.

Supplementary Figures

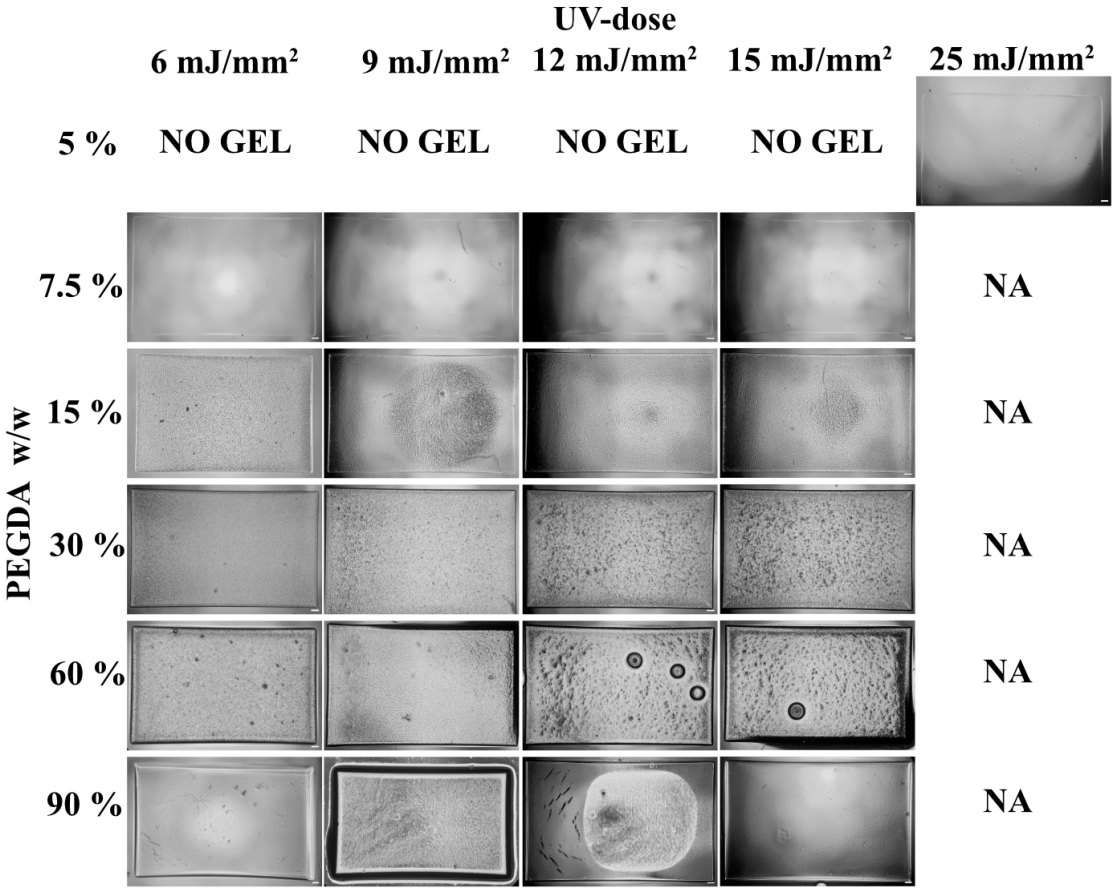

Supplementary Figure 1: Extended screening of PEGDA polymerization across concentration and UV dose.

Brightfield overview of PEGDA hydrogels fabricated using the LigHTS workflow[9] across a broad concentration range (5-90% w/w) and increasing UV doses (6-25 mJ/mm^2). The matrix highlights the progressive emergence of optical turbidity and microdomain formation at intermediate polymer concentrations, as well as cracking and delamination at very high PEGDA content. The dataset complements the main figure by providing a complete visualization of formulation-dependent variability in optical homogeneity and structural integrity. NA means the dose was not tested for the specific hydrogel formulation.

Scale bars: 100 µm.

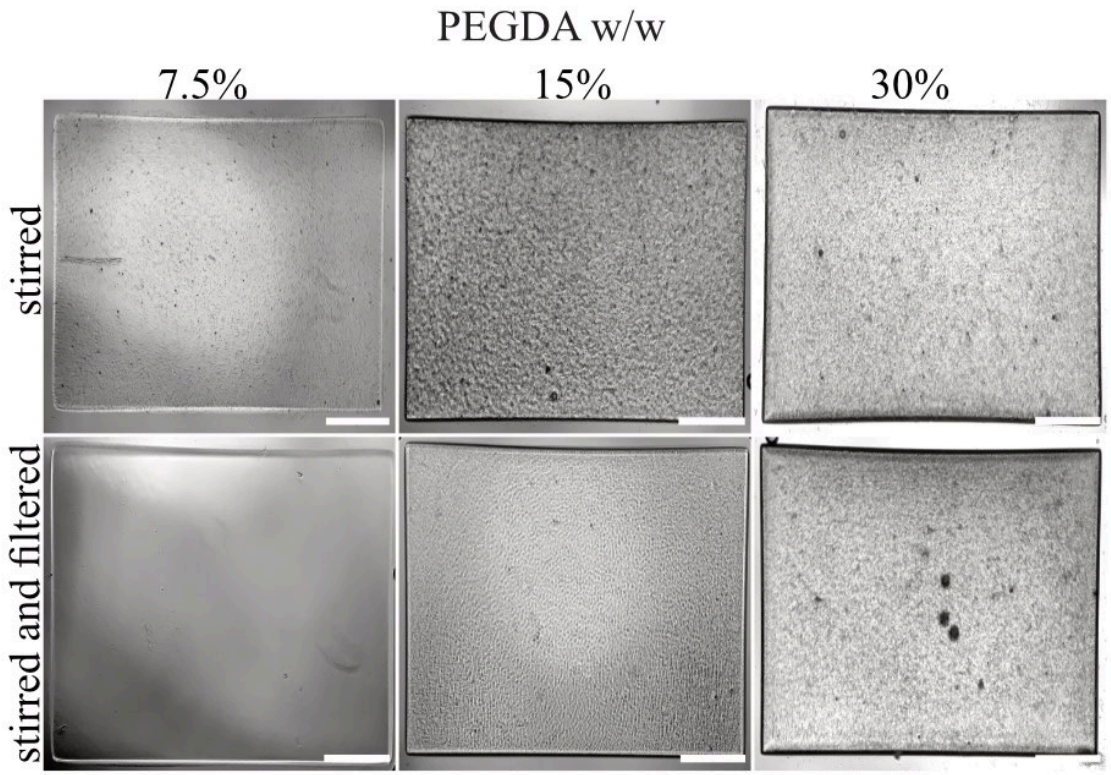

Supplementary Figure 2: Stirring and sterile filtering improved optical clarity in PEGDA hydrogels.

Representative brightfield images of flat PEGDA hydrogels fabricated from precursor solutions prepared by stirring or by stirring followed by sterile filtration. PEGDA concentrations of 7.5% w/w, 15% w/w, and 30% w/w were tested. Hydrogels were fabricated using the LigHTS [9] photopatterning workflow, maintaining tartrazine at 4.5 mg/mL and LAP at 1 mg/mL. Flat gels were produced using PRIMO (Alvéole) photopatterning with a uniform UV exposure dose of 8 mJ/mm^2.

(a-b) 7.5% w/w PEGDA; (c-d) 15% w/w PEGDA, (e-f) 30% w/w PEGDA. Filtration improves optical clarity at low and intermediate PEGDA concentrations, while high PEGDA concentration remains optically opaque. Scale bar: 500 µm.

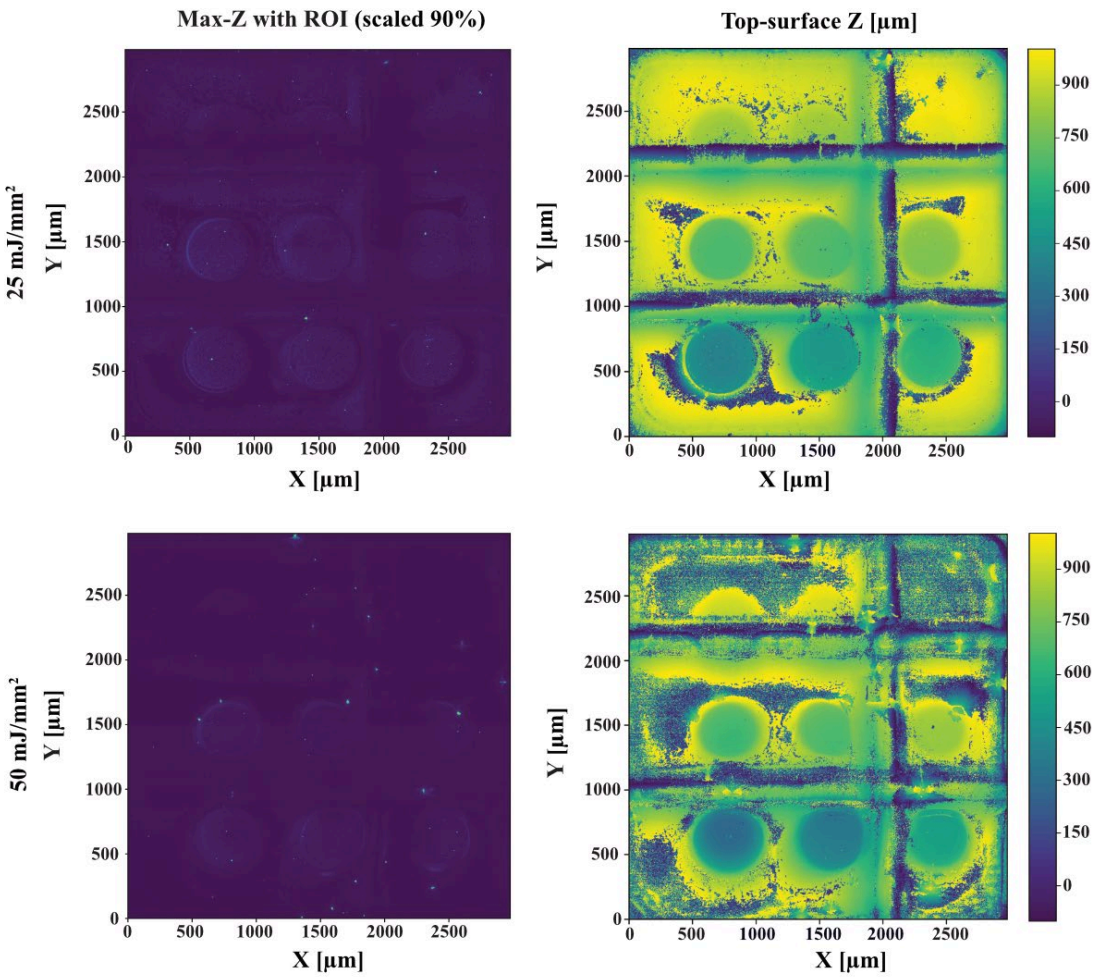

Supplementary Figure 3: expanded visualization of top-surface Z reconstructions across 25 mJ/mm² and 50 mJ/mm² exposure dose.

Expanded visualization of top-surface Z reconstructions and corresponding residual maps for all UV exposure conditions. The data highlight a transition from relatively smooth surfaces at low exposure to highly heterogeneous and saturated profiles at high exposure, consistent with over-polymerization and reduced grayscale fidelity.

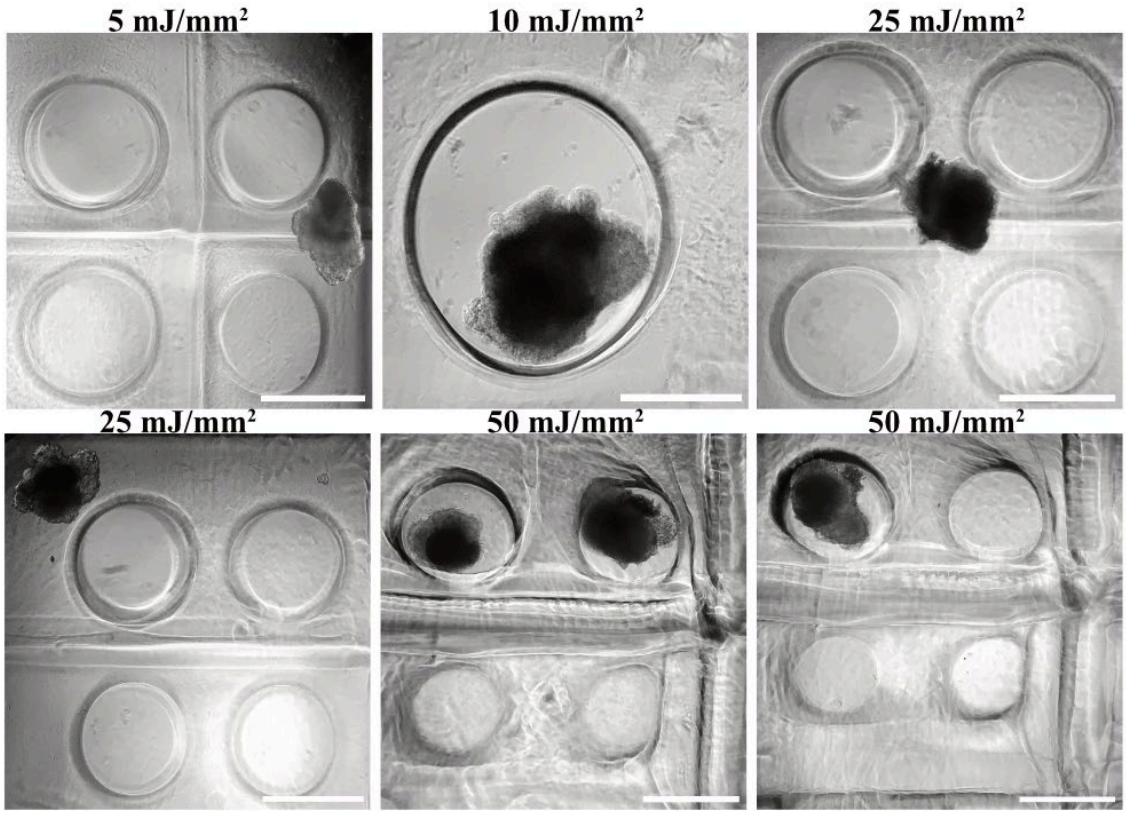

Supplementary Figure 4: Brightfield visualization of cardioid seeding outcomes in the first housing design at increasing UV exposure doses.

Representative brightfield images of cardioids seeded onto PEGDA slots fabricated at nominal UV doses of 5 mJ/mm^2, 10 mJ/mm^2, 25 mJ/mm^2, and 50 mJ/mm^2. At low exposure doses (5 mJ/mm^2 and 10 mJ/mm^2), cavities are shallow, and cardioids remain on the gel surface or partially engage the slot. Intermediate exposure (25 mJ/mm^2) produces deeper cavities but does not reliably promote complete cardioid entry. Only at the highest exposure (50 mJ/mm^2) do cardioids consistently settle within the slots; however, this condition is associated with pronounced fabrication artifacts, including stitching and surface deformation, which compromise optical quality.

Scale bars: 500 μm.

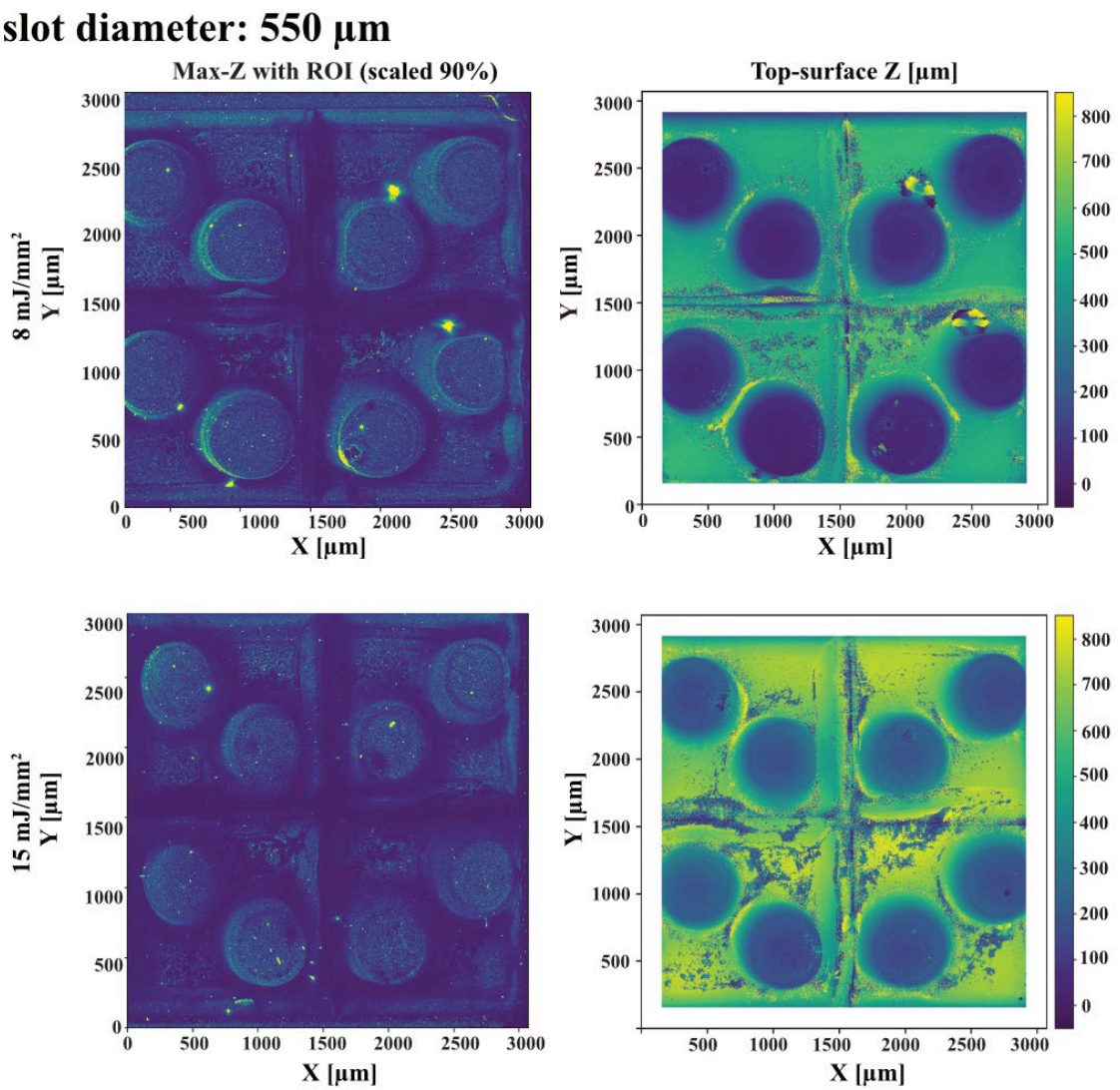

Supplementary Figure 5: Quantitative top-surface characterization of optimized slot structures (550 µm diameter).

Topographical reconstruction of PEGDA cavities with a nominal diameter of 550 µm fabricated at 8 mJ/mm^2 and 15 mJ/mm^2.

Left panels: maximum-Z projection with scaled 90% ROI used for analysis.

Centre panels: reconstructed top-surface height maps (top-surface Z, µm) obtained by identifying the axial position of maximum fluorescence intensity at each (x,y) coordinate.

Compared to the first slots design, stitching artifacts were markedly reduced, confirming improved grayscale fidelity at imaging-compatible UV doses.

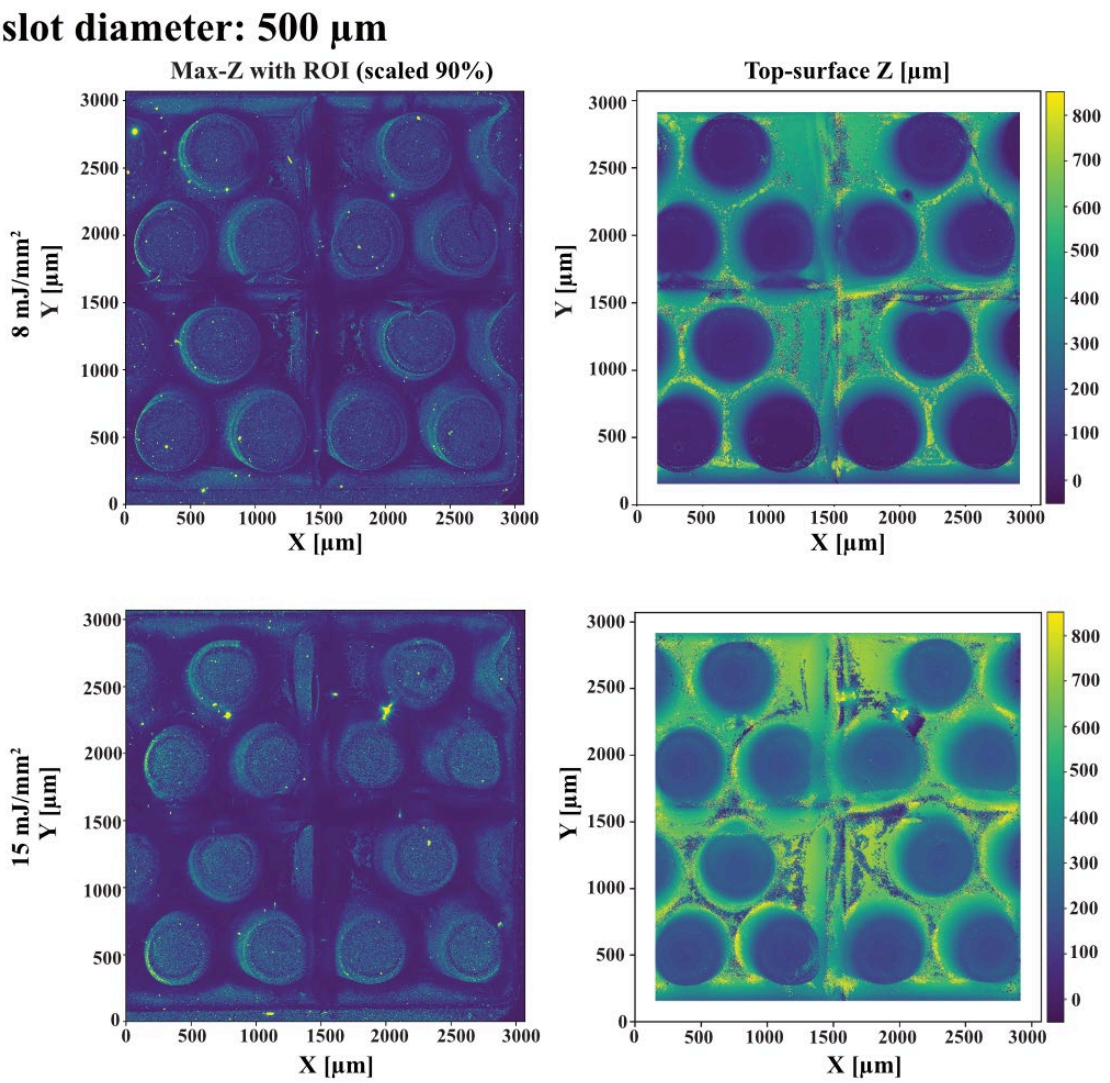

Supplementary Figure 6: Quantitative top-surface characterization of optimized housing structures (500 µm diameter).

Topographical reconstruction of PEGDA cavities with a nominal diameter of 500 µm fabricated at 8 mJ/mm^2 and 15 mJ/mm^2.

As in **Supplementary Figure 5** , we used maximum-Z projections and reconstructed top-surface maps. Both doses yielded symmetric cavities with well-defined funnel profiles.

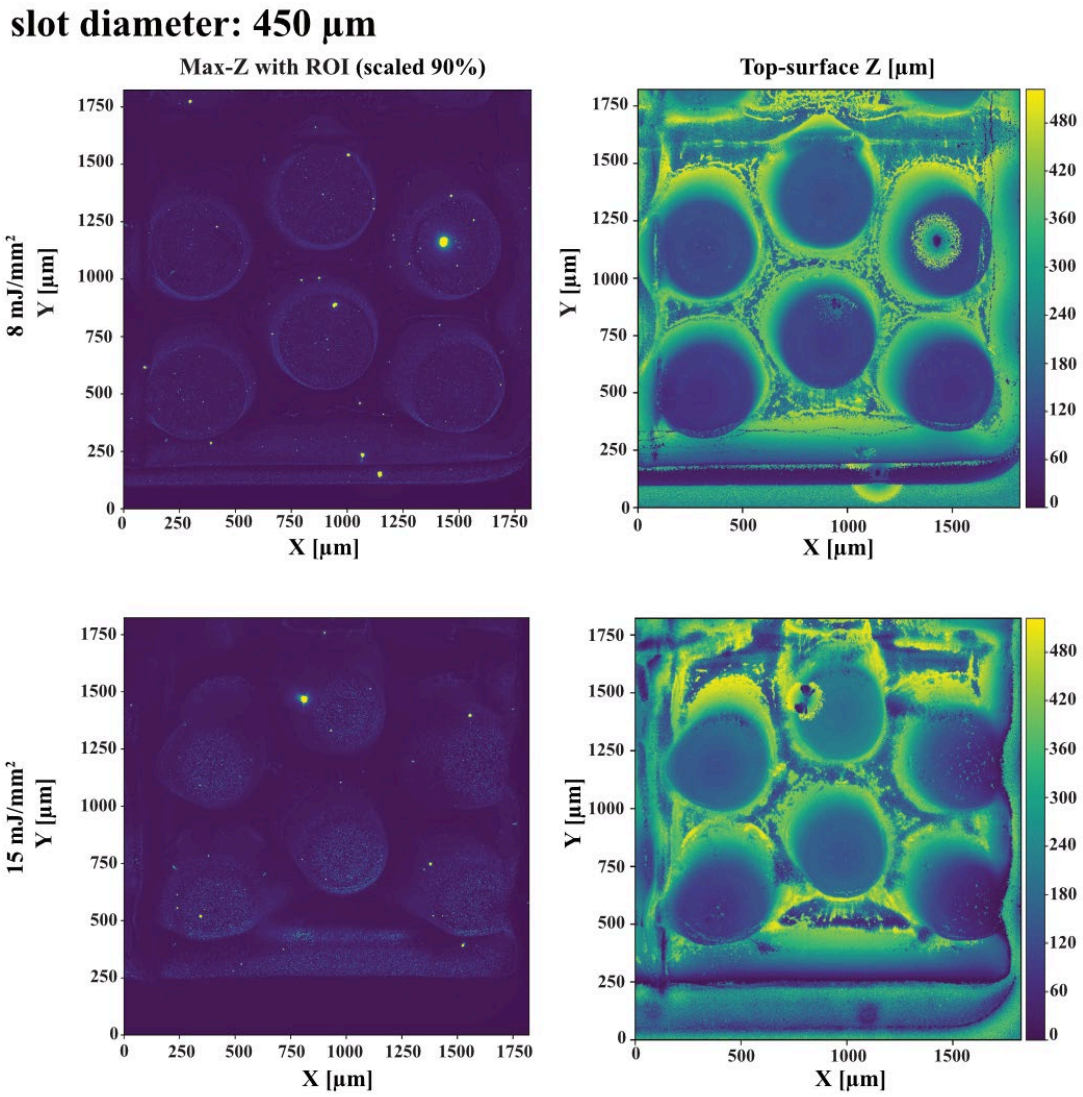

Supplementary Figure 7: Top-surface reconstruction of 450 µm diameter cavities.

Topographical reconstruction of PEGDA cavities with a nominal diameter of 450 µm fabricated at 8 mJ/mm^2 and 15 mJ/mm^2.

Left panels show maximum-Z projections with the scaled region of interest (ROI, 90% of patterned area). Right panels report reconstructed top-surface height maps (Top-surface Z, µm) obtained from confocal z-stacks by pixel-wise identification of the gel-glass interface.

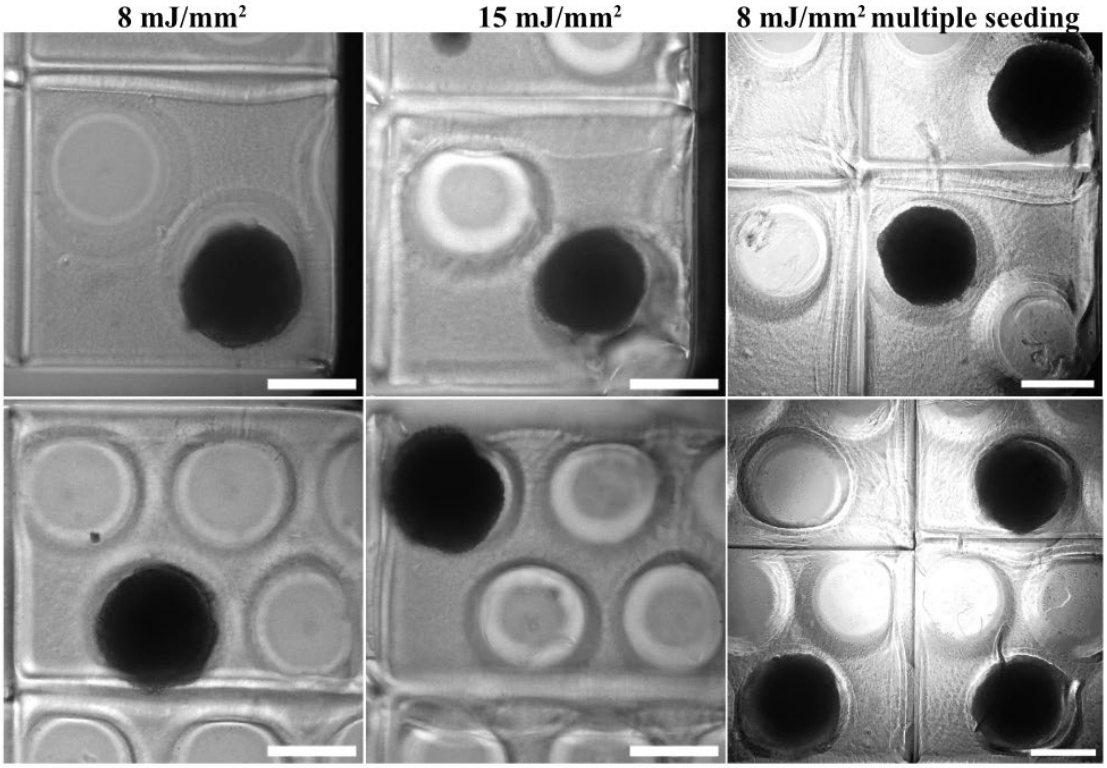

Supplementary Figure 8: Dose-dependent morphology and passive seeding behavior across gradient cavity designs.

Brightfield overview of different patterned PEGDA cavities (550 µm and 500 µm) fabricated at different UV doses (8 mJ/mm^2 and 15 mJ/mm^2) and under multiple seeding conditions. Lower doses preserved optical clarity while maintaining adequate cavity contrast, whereas higher doses increased vertical relief but introduced local geometric distortions. Scale bar: 500 µm.

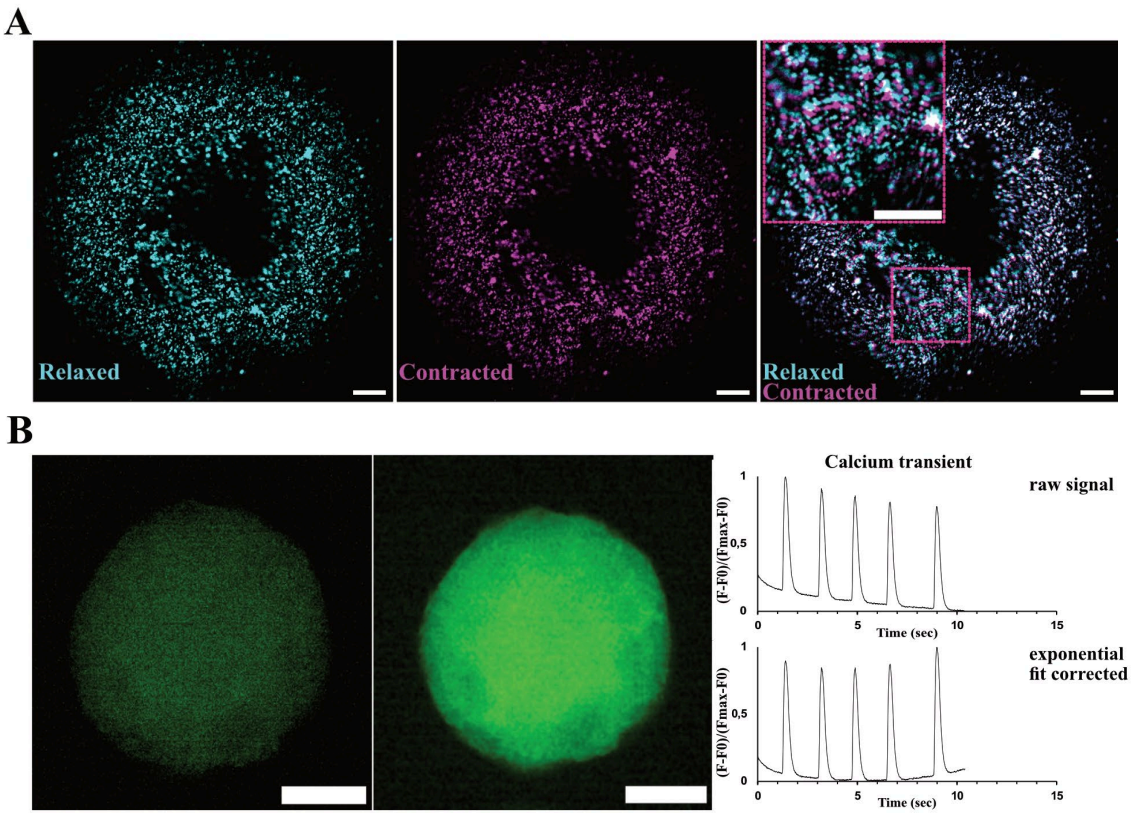

Supplementary Figure 9: Beads displacement and physiological validation of PEGDA-supported cardioids.

(A) Fluorescent bead configuration at the gel-cardioid interface in relaxed (cyan) and contracted (magenta) states. The overlay highlights bead displacement within the mechanically active region used for TFM analysis; **(B)** representative calcium transient recordings from cardioids cultured on PEGDA substrates. Raw fluorescence signal (top) and exponential baseline-corrected trace (bottom) show preserved rhythmic activity, confirming that substrate compliance does not impair excitation-contraction coupling. Scale bar: 20 µm.

Bibliography

1. *Cardiovascular Diseases (CVDs)*. https://www.who.int/news-room/fact-sheets/detail/cardiovascular-diseases-(cvds).
2. 2024 Heart Disease and Stroke Statistics: A Report of US and Global Data From the American Heart Association. https://www.ahajournals.org/doi/10.1161/CIR.0000000000001209.
3. Prondzynski, M. *et al.* Efficient and reproducible generation of human iPSC-derived cardiomyocytes and cardiac organoids in stirred suspension systems. *Nat Commun* **15**, 5929 (2024).
4. Schmidt, C. *et al.* Multi-chamber cardioids unravel human heart development and cardiac defects. *Cell* **186**, 5587-5605.e27 (2023).
5. Torchia, E. *et al.* Fabrication of cell culture hydrogels by robotic liquid handling automation for high-throughput drug testing. *Commun Eng* **4**, 222 (2025).
6. Lannou, S. *et al.* The Public Health Burden of Cardiomyopathies: Insights from a Nationwide Inpatient Study. *JCM* **9**, 920 (2020).
7. Harrer, S., Shah, P., Antony, B. & Hu, J. Artificial Intelligence for Clinical Trial Design. *Trends in Pharmacological Sciences* **40**, 577–591 (2019).
8. Kim, J., Koo, B.-K. & Knoblich, J. A. Human organoids: model systems for human biology and medicine. *Nat Rev Mol Cell Biol* **21**, 571–584 (2020).
9. Enrico, A., Rigolli, S., Zimmermann, J. & Pezzotti, M. LigHTS: Massively Parallel Biomimetic Photo-Functionalization for Imaging-Based Ultra-High-Throughput Screening.

10. Pezzotti, M., Torchia, E., Zimmermann, J., Rigolli, S. & Enrico, A. Vertically Integrated System for Tracking and Assessing cell-cycle aware phenotypes under confinement.

11. Nerger, B. A., Siedlik, M. J. & Nelson, C. M. Microfabricated tissues for investigating traction forces involved in cell migration and tissue morphogenesis. *Cell. Mol. Life Sci.* **74**, 1819–1834 (2017).

12. Balmas, E. *et al.* Single Cell Transcriptional Perturbome in Pluripotent Stem Cell Models. Preprint at https://doi.org/10.2139/ssrn.4854180 (2024).

13. Notbohm Research Group. Cell Traction and Monolayer Stress Microscopy MATLAB package.

14. Lewis-Israeli, Y. R. *et al.* Self-assembling human heart organoids for the modeling of cardiac development and congenital heart disease. *Nat Commun* **12**, 5142 (2021).

15. Hofbauer, P. *et al.* Cardioids reveal self-organizing principles of human cardiogenesis. *Cell* **184**, 3299-3317.e22 (2021).

16. Di Sante, M. *et al.* CALIPERS: Cell cycle-aware live imaging for phenotyping experiments and regeneration studies. Preprint at https://doi.org/10.1101/2024.12.19.629259 (2024).

17. Hamad, S. *et al.* Generation of human induced pluripotent stem cell-derived cardiomyocytes in 2D monolayer and scalable 3D suspension bioreactor cultures with reduced batch-to-batch variations. *Theranostics* **9**, 7222–7238 (2019).

18. Zhang, C. *et al.* Dynamic hydrogel mechanics in organoid engineering: From matrix design to translational paradigms. *Bioactive Materials* **55**, 144–170 (2026).

19. Li, Y. *et al.* The molecular mechanisms of cardiac development and related diseases. *Sig Transduct Target Ther* **9**, 368 (2024).

20. Tsan, Y.-C. *et al.* Physiologic biomechanics enhance reproducible contractile development in a stem cell derived cardiac muscle platform. *Nat Commun* **12**, 6167 (2021).

21. Cassel De Camps, C. *et al.* Hydrogel Mechanics Influence the Growth and Development of Embedded Brain Organoids. *ACS Appl. Bio Mater.* **5**, 214–224 (2022).

22. Lai, W., Geliang, H., Bin, X. & Wang, W. Effects of hydrogel stiffness and viscoelasticity on organoid culture: a comprehensive review. *Mol Med* **31**, 83 (2025).

23. Cho, Y., You, J. & Lee, J. H. Natural Polymer-Based Hydrogel Platforms for Organoid and Microphysiological Systems: Mechanistic Insights and Translational Perspectives. *Polymers* **17**, 2109 (2025).

24. Hakim Khalili, M. *et al.* Additive Manufacturing and Physicomechanical Characteristics of PEGDA Hydrogels: Recent Advances and Perspective for Tissue Engineering. *Polymers* **15**, 2341 (2023).

25. Caliari, S. R. & Burdick, J. A. A practical guide to hydrogels for cell culture. *Nat Methods* **13**, 405–414 (2016).

26. Song, Y. *et al.* Mechanically and Chemically Defined PEG Hydrogels Improve Reproducibility in Human Cardioid Development. *Adv Healthcare Materials* **14**, 2403997 (2025).

27. Dembo, M. & Wang, Y.-L. Stresses at the Cell-to-Substrate Interface during Locomotion of Fibroblasts. *Biophysical Journal* **76**, 2307–2316 (1999).

28. Butler, J. P., Tolić-Nørrelykke, I. M., Fabry, B. & Fredberg, J. J. Traction fields, moments, and strain energy that cells exert on their surroundings. *American Journal of Physiology-Cell Physiology* **282**, C595–C605 (2002).

29. Denisin, A. K., Kim, H., Riedel-Kruse, I. H. & Pruitt, B. L. Field Guide to Traction Force Microscopy. *Cel. Mol. Bioeng.* **17**, 87–106 (2024).

30. Zancla, A., Mozetic, P., Orsini, M., Forte, G. & Rainer, A. A primer to traction force microscopy. *Journal of Biological Chemistry* **298**, 101867 (2022).

31. Barrasa-Fano, J. *et al.* Guidance for 3D traction force microscopy today and in the next decade. *Nat Methods* https://doi.org/10.1038/s41592-025-02934-6 (2025) doi:10.1038/s41592-025-02934-6.

32. Trepat, X. *et al.* Physical forces during collective cell migration. *Nature Phys* **5**, 426–430 (2009).

33. Tambe, D. T. *et al.* Collective cell guidance by cooperative intercellular forces. *Nature Mater* **10**, 469–475 (2011).

34. Cheung, B. C. H., Abbed, R. J., Wu, M. & Leggett, S. E. 3D Traction Force Microscopy in Biological Gels: From Single Cells to Multicellular Spheroids. *Annual Review of Biomedical Engineering* **26**, 93–118 (2024).

35. Balmas, E. *et al.* Single Cell Transcriptional Perturbome in Pluripotent Stem Cell Models. Preprint at https://doi.org/10.2139/ssrn.4854180 (2024).

36. Del Álamo, J. C. *et al.* Spatio-temporal analysis of eukaryotic cell motility by improved force cytometry. *Proc. Natl. Acad. Sci. U.S.A.* **104**, 13343–13348 (2007).

37. Huang, Y. *et al.* Traction force microscopy with optimized regularization and automated Bayesian parameter selection for comparing cells. *Sci Rep* **9**, 539 (2019).

38. Huang, Y., Gompper, G. & Sabass, B. A Bayesian traction force microscopy method with automated denoising in a user-friendly software package. *Computer Physics Communications* **256**, 107313 (2020).

39. Schmidt, C. *et al.* Multi-chamber cardioids unravel human heart development and cardiac defects. *Cell* **186**, 5587-5605.e27 (2023).

40. Feng, Y., Ringeisen, N., Dufresne, E. R., Isa, L. & Style, R. W. Controlling polymerization-induced phase separation in the synthesis of porous gels. Preprint at https://doi.org/10.48550/arXiv.2508.15571 (2025).

41. Legant, W. R. *et al.* Measurement of mechanical tractions exerted by cells in three-dimensional matrices. *Nat Methods* **7**, 969–971 (2010).

Table of figures